Bralower, T.J., Premoli Silva, I., Malone, M.J., et al., 2002
Proceedings of the Ocean Drilling Program, Initial Reports Volume 198

2. Explanatory Notes[1]

Shipboard Scientific Party[2]

INTRODUCTION

Information assembled in this chapter will help the reader understand the basis for our preliminary conclusions and also enable the interested investigator to select samples for further analysis. This information concerns only shipboard operations and analyses described in the site reports in the Leg 198 *Initial Reports* volume of the *Proceedings of the Ocean Drilling Program*. Methods used by various investigators for shore-based analyses of Leg 198 data will be described in the individual contributions published in the *Scientific Results* volume and in publications in various professional journals.

Authorship of Site Chapters

The separate sections of the site chapters were written by the following shipboard scientists (authors are listed in alphabetical order; no seniority is implied):

Principal Results: Shipboard Scientific Party
Background and Objectives: Bralower, Premoli Silva
Operations: Malone, Storms
Lithostratigraphy: Arthur, Dutton, Gylesjö, Hancock, Kano, Marsaglia, Thomas, Zachos
Biostratigraphy: Bown, Bralower, Eleson, Kano, Leckie, Petrizzo, Premoli Silva, Takeda
Paleomagnetism: Channell, Sager
Composite Depths: McGuire, Röhl
Sedimentation and Accumulation Rates: Frank, Leckie
Organic Geochemistry: Brassell
Inorganic Geochemistry: Averyt, Frank

[1]Examples of how to reference the whole or part of this volume.
[2]Shipboard Scientific Party addresses.

Ms 198IR-102

Physical Properties: Clarke, McGuire, Röhl, Robinson
Downhole Measurements: Moe, Williams

Drilling Operations

Three standard coring systems were used during Leg 198: the advanced piston corer (APC), the extended core barrel (XCB), and the rotary core barrel (RCB). These standard coring systems and their characteristics are summarized in the "Explanatory Notes" chapters of various previous *Initial Reports* volumes as well a number of technical notes. The Leg 139 *Initial Reports* volume (Davis, Mottle, Fisher, et al., 1992) includes a particularly detailed description. In addition, the motor driven core barrel (MDCB) system was deployed in an attempt to improve recovery in alternating chert/chalk layers. All systems were applied to maximize recovery of the sediments cored. Most cored intervals were ~9.6-m long, which is the length of a standard core barrel. However, the MDCB system cores 4.5-m intervals. In other cases, the drill string was drilled, or "washed ahead," without recovering sediments to advance the drill bit to a target depth where core recovery needed to be resumed.

Drilled intervals are referred to in meters below rig floor (mbrf), which are measured from the kelly bushing on the rig floor to the bottom of the drill pipe, and meters below seafloor (mbsf), which are calculated. When sediments of substantial thickness cover the seafloor, the mbrf depth of the seafloor is determined with a mudline core, assuming 100% recovery for the cored interval in the first core. Water depth is calculated by subtracting the distance from the rig floor to sea level from the mudline measurement in mbrf. This water depth usually differs from precision depth recorder measurements by a few to several meters. The mbsf depths of core tops are determined by subtracting the seafloor depth (in mbrf) from the core-top depth (in mbrf). The resulting core-top datums in mbsf are the ultimate reference for any further depth calculation procedures.

Drilling Deformation

When cores are split, many show signs of significant sediment disturbance, including the concave-downward appearance of originally horizontal bedding, haphazard mixing of lumps of different lithologies (mainly at the tops of cores), fluidization, and flow-in. Core deformation may also occur during retrieval because of changes in pressure and temperature as the core is raised, and during cutting and core handling on deck.

Curatorial Procedures and Sample Depth Calculations

Numbering of sites, holes, cores, and samples follows the standard Ocean Drilling Program (ODP) procedure. A full curatorial identifier for a sample consists of the leg, site, hole, core number, core type, section number, and interval in centimeters measured from the top of the core section. For example, a sample identification of 198-1207A-1H-1, 10–12 cm, represents a sample removed from the interval between 10 and 12 cm below the top of Section 1, Core 1 (H designates that this core was taken with the APC system) of Hole 1207A during Leg 198. Cored intervals are also referred to in "curatorial" mbsf. The mbsf of a sample is calculated by adding the depth of the sample below the section top and

the lengths of all higher sections in the core to the core-top datum measured with the drill string.

A sediment core from less than a few hundred mbsf, in some cases, may expand upon recovery (typically 10% in the upper 300 mbsf), and its length may not necessarily match the drilled interval. In addition, a coring gap typically occurs between cores, as shown by composite depth construction (see the Legs 138, 177, and 189 *Initial Reports* volumes [Shipboard Scientific Party, 1992, 1999, 2001]). Thus, a discrepancy may exist between the drilling mbsf and the curatorial mbsf. For instance, the curatorial mbsf of a sample taken from the bottom of a core may be larger than that of a sample from the top of the subsequent core, where the latter corresponds to the drilled core-top datum.

If a core has incomplete recovery, all cored material is assumed to originate from the top of the drilled interval as a continuous section for curation purposes. The true depth interval within the cored interval is not known. This should be considered as a sampling uncertainty in age-depth analysis and correlation of core facies with downhole log signals.

Core Handling and Analysis

General core handling procedures are described in previous *Initial Reports* volumes and the *Shipboard Scientist's Handbook* and are summarized here. As soon as cores arrived on deck, gas void samples (if present) were taken by means of a syringe for immediate analysis as part of the shipboard safety and pollution prevention program. Core catcher samples were obtained for biostratigraphic analysis. When the core was cut in sections, whole-round samples were taken for shipboard interstitial water analysis. In addition, headspace gas samples were immediately extracted from the ends of cut sections and sealed in glass vials for light hydrocarbon analysis.

Before splitting, whole-round core sections were run through the multisensor track (MST), and thermal conductivity measurements were taken. The cores were then split into working and archive halves (from bottom to top), so investigators should be aware that older material could have been transported upward on the split face of each section. When short pieces of sedimentary rock were recovered, the individual pieces were split with the rock saw and placed in split liner compartments created by sealing spacers into the liners with acetone.

Coherent and reasonably long archive-half sections were measured for color reflectance using the archive multisensor track (AMST). All archive-half sections were run through the cryogenic magnetometer, described visually and by means of smear slides and thin sections, and photographed with both black-and-white and color film. Close-up photographs were taken of particular features for illustrations in site chapters, as requested by individual scientists. During Leg 198, a digital imaging track system equipped with a line-scan camera was installed for the first time and used extensively.

The working half was sampled both for shipboard analysis—such as physical properties, carbonate, and bulk X-ray diffraction (XRD) mineralogy—and for shore-based studies. Both halves of the core were then put into labeled plastic tubes, sealed, and placed in a cold-storage space aboard the ship. At the end of the leg, the cores were transferred from the ship into refrigerated containers and shipped to the ODP Gulf Coast Core Repository in College Station, Texas.

LITHOSTRATIGRAPHY

Sediment Barrel Sheets

Core description forms, or "barrel sheets," provide a summary of the data obtained during shipboard analysis of each sediment core. Detailed observations of each section were recorded initially by hand on standard ODP Visual Core Description (VCD) forms. Copies of original VCD forms are available from ODP upon request. This information was subsequently entered into AppleCORE (version 8.1m) software, which generates a simplified, annotated graphical description (barrel sheet) for each core. These barrel sheets appear alongside corresponding core photographs (see the "Core Descriptions" contents list). Site, hole, and depth in mbsf are given at the top of the barrel sheet, with mbsf positions of core sections indicated along the left margin. Columns on the barrel sheets include graphic lithology, bioturbation, sedimentary structures, accessory lithologies, fossils, sediment disturbance, sample types, and remarks. These columns are discussed below, followed by an outline of the lithostratigraphic classification used during Leg 198.

Graphic Lithology

Lithologies of the core intervals recovered are represented on barrel sheets by graphic patterns in the column titled "Graphic Lithology" (Fig. F1). For intervals containing homogeneous mixtures of multiple lithologies, symbols are arranged within the column from left to right in order of their relative abundance. Graphic lithologies are used for all components that comprise 25% or greater of the total sediment. The width of each pattern in the column approximates the relative abundance of that component. Relative abundances reported in this volume are useful for general characterization of the sediment, but they are not precise, quantitative data.

F1. Key to symbols in graphic lithology column log, computer-generated core description forms, p. 42.

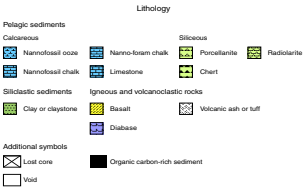

Sedimentary Structures

Sedimentary structures formed by natural processes and not as a result of drilling disturbance are represented on the barrel sheet under the "Sedimentary Structures" column (Fig. F2). Structures formed by both biogenic and physical processes are included. These include varying degrees of bioturbation, types of trace fossils, parallel laminations, and soft sediment deformation structures.

Bioturbation

Using a scheme similar to that proposed by Droser and Bottjer (1986), five levels of bioturbation were recognized. Bioturbation intensity was classified as abundant (≥75%), common (50%–<75%), moderate (10%–<50%), rare (<10%), and barren (none); these levels were illustrated with graphic symbols in the "Bioturbation" column (Fig. F2).

Accessory Features

Symbols are used to denote accessory lithologies, authigenic minerals, concretions, fossils, and sediment disturbance induced by the coring process (Fig. F2). Symbols are positioned at the location in the section where that feature is observed. If the feature extends over an

F2. Key to symbols for contacts, physical structures, lithologic accessories, ichnofossils, fossils, core-disturbance, and bioturbation, computer-generated core description forms, p. 43.

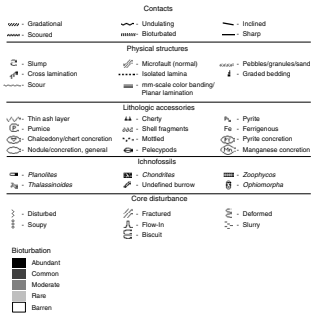

interval, the symbol appears centered on a vertical line to denote the stratigraphic extent of occurrence.

Color

Colors were determined qualitatively using the Munsell rock color charts (Rock-Color Chart Committee, 1991) and, to avoid color changes associated with drying and redox reactions, were described immediately after the cores were split.

Sample Types

Sample material taken for shipboard sedimentologic and chemical analysis consisted of pore water whole-round samples, "toothpick" samples (smear slides), thin section billets, and discrete samples for XRD and coulometric analysis. Typically, two to three smear slides (or thin sections) were made per core, one pore water, and two coulometer samples taken per core. XRD samples were taken only where needed to assess the lithologic components. Additional samples were selected to better characterize lithologic variability within a given interval. Tables summarizing data, such as grain size and relative abundance of sedimentary components from smear slides, were generated using a spreadsheet program (Sliders).

Remarks

The written description for each core contains a brief overview of major and minor lithologies that are present, as well as notable features (e.g., sedimentary structures).

Sediment Classification

Lithologic names consist of a principal name based on composition, degree of lithification, and/or texture as determined from visual description and smear slide observations. For a mixture of components, the principal name is preceded by major modifiers (in order of increasing abundance) that refer to components making up ≥25% of the sediment. Minor components that represent between 10% and 25% of the sediment follow the principal name after a "with" in order of increasing abundance. Thus, an unconsolidated sediment containing 30% nannofossils, 25% clay minerals, 20% foraminifers, 15% quartz silt, and 10% manganese nodules would be described as a clayey nannofossil ooze with manganese nodules, quartz silt, and foraminifers. Sedimentary components ranging from 10% to 25% were reflected in the sediment name in the description column as "WITH," but these components were not designated in the graphic lithology column. These naming conventions follow the ODP sediment classification scheme (Mazzullo et al., 1988), with the exception that during Leg 198 a separate "mixed sediment" category was not distinguished. During Leg 198, we did not encounter neritic sediments or chemical sediments except as accessory minerals and do not address these categories below.

Sediment was classified on the basis of composition estimated by visual examination of the core, smear slides, and thin sections, and by shipboard measurements of carbonate content (see **"Carbonate Analysis,"** p. 19, in "Organic Geochemistry") and shipboard XRD analyses (see **"X-Ray Diffraction,"** p. 9). In volcaniclastic sediments, the term

"ash" (or "tuff" if lithified) is used in place of "sand," whereas "lapilli" is used for granule and cobble size categories. Larger volcanic clasts (breccia) were not encountered, but discrete pumice lapilli are noted as "pumice clasts." Size divisions for grains are those of Wentworth (1922) (Fig. F3). Size-textural qualifiers were not used for pelagic sediment names (e.g., nannofossil clay implies that the dominant component is detrital clay rather than clay-sized nannofossils).

Terms that describe lithification vary depending upon the dominant composition:

1. Sediment derived predominantly from calcareous pelagic organisms (e.g., calcareous nannofossils and foraminifers): The lithification terms "ooze," "chalk," and "limestone" reflect whether the sediment can be deformed with a finger (ooze), can be scratched easily by a fingernail (chalk), or cannot be scratched easily (limestone).
2. Sediment derived predominantly from siliceous microfossils (diatoms, radiolarians, and siliceous sponge spicules): The lithification terms "ooze," "radiolarite/spiculite/diatomite," "porcellanite," and "chert" reflect whether the sediment can be deformed with a finger (ooze), cannot be easily deformed manually (radiolarite/spiculite/diatomite), or displays a glassy luster (chert). We use the term "porcellanite" as defined by Keene (1975) to describe a siliceous limestone/claystone that has a dull luster and is less hard and compact than chert. It may contain a mix of opal, quartz, clay minerals, and carbonate. Note that the terms "porcellanite" and "chert" do not imply crystallinity of the silica.
3. Sediment derived predominantly from siliciclastic material: If the sediment can be deformed easily with a finger, no lithification term is added and the sediment is named for the dominant grain size. For more consolidated material, the lithification suffix "-stone" is appended to the dominant size classification (e.g., "clay" vs. "claystone").
4. Sediment composed of sand-sized volcaniclastic grains: If the sediment can be deformed easily with a finger, the interval is described as ash. For more consolidated material, the rock is called tuff. The term "lapilli" is used for coarse-grained material.

F3. Grain-size divisions, sedimentary rocks, p. 44.

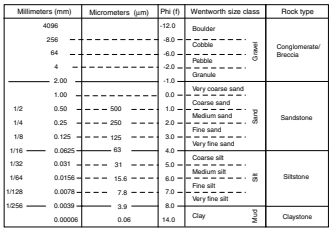

Color Reflectance Spectrophotometry

In addition to visual estimates of the color, reflectance of visible light from soft sediment cores was routinely measured using a Minolta spectrophotometer (model CM-2002) mounted on the AMST. The AMST measures the archive half of each core section and provides a high-resolution stratigraphic record of color variations for visible wavelengths (400–700 nm). Freshly split cores were covered with clear plastic wrap and placed on the AMST. Measurements were taken at 2.5 cm spacing. The AMST skips empty intervals and intervals where the core surface is well below the level of the core liner, but the AMST cannot recognize relatively small cracks or disturbed areas of core. Thus, AMST data may contain spurious measurements that should, to the extent possible, be edited out of the data set before use. Each measurement recorded consists of 31 separate determinations of reflectance in 10-nm-wide spectral bands from 400 to 700 nm. Additional detailed information about measurement and interpretation of spectral data with the

Minolta spectrophotometer can be found in Balsam et al. (1997, 1998) and Balsam and Damuth (2000).

Core Curation and Shipboard Sampling of Igneous Rocks

To describe important mineralogic and structural features in both the archive and working halves, we examined core sections containing igneous rocks prior to cutting with a diamond-impregnated saw. Each piece was numbered sequentially from the top of the core section and labeled on the outside surface. Pieces that could be fit together were assigned the same number and were lettered consecutively (e.g., 1A, 1B, 1C, etc.). Plastic spacers were placed between pieces with different numbers. The presence of a spacer may represent a substantial interval of no recovery. If it was evident that an individual piece had not rotated about a horizontal axis during drilling, an arrow pointing to the top of the section was added.

Nondestructive physical properties measurements, such as natural gamma ray emission, were made on the core before it was split (see **"Physical Properties,"** p. 22). After the core was split, lithologic descriptions were made of the archive half and the working half was sampled for shipboard physical properties measurements (see **"Physical Properties,"** p. 22), thin sections, and XRD. The archive half was described on the VCD form and was imaged and then photographed.

Visual Core Descriptions and Barrel Sheets for Igneous Rocks

We used VCD forms to document each section of the igneous rock cores. The left column on the form represents the archive half. A horizontal line across the entire width of the column denotes a plastic spacer. Oriented pieces are indicated on the form by an upward-pointing arrow to the right of the piece. Locations of samples selected for shipboard studies are indicated in the column headed "Shipboard Studies," with the following notation: XRD = X-ray diffraction analysis and TSB = thin section billet. Core summaries of VCD descriptions for each core were produced in AppleCORE. Copies of VCDs are available from ODP upon request.

We subdivided the core into consecutively numbered lithologic units (denoted in the "Lithologic Unit" column on the VCD) on the basis of changes in color, structure, brecciation, grain size, vesicle abundance, mineral occurrence and abundance, and the presence of sedimentary interbeds. Intercalated sediment horizons were designated as "A" and the underlying volcanic rock as "B" within the same unit.

Written descriptions accompany the schematic representation of the core sections and include the following:

1. The leg, site and hole, core, type and section number (e.g., 197-1203A-15R-3), as well as the top of the core section measured in mbsf.
2. The unit number (consecutive downhole), the rock name (see below) and the piece numbers. We assigned provisional rock names on the basis of hand specimen observation (hand lens and binocular microscope) and later checked these assignments by examining thin sections. The following notation is used: ho-

locrystalline (90%–100% crystals); hypocrystalline (50%–<90% crystals); hypohyaline (10%–<50% crystals); and holohyaline (<10% crystals). Porphyritic rocks were named by phenocryst type; the term "phenocryst" was used for a crystal that was significantly (typically five times) larger than the average size of the groundmass crystals and/or generally euhedral in shape. This nomenclature is sensitive to changes in the groundmass grain size. A visual estimation of abundance and variation of phenocrysts within the basalt intervals was made using the following terms: aphyric (phenocryst content is <1%); sparsely phyric (phenocryst content is 1%–2%); moderately phyric (phenocryst content is >2%–10%); and highly phyric (phenocryst content is >10%).

3. Contact relations and unit boundaries. After we made lithologic descriptions, we attempted to integrate the observations to define unit boundaries. Boundaries often reflect major physical changes in the core (e.g., pillowed vs. massive). Intervals of sediment and/or hyaloclastite, changes in vesicularity, alteration, volume fraction, and type of matrix.
4. Phenocrysts. This entry describes the types of minerals visible with a hand lens or binocular microscope and their distribution within the unit, as well as each phase's abundance (in volume percent), size range (in millimeters), shape, and degree of alteration, with additional comments if appropriate.
5. Groundmass texture and grain size: glassy, aphanitic, fine-grained (<1 mm), medium-grained (1–5 mm), or coarse-grained (>5 mm). Changes in grain size and proportions of crystals and glass within units were also noted.
6. Vesicles. This entry records vesicle abundance (visual estimates of the volume fraction of vesicles were supplemented by observations using a binocular microscope), size, shape (sphericity and angularity), and whether the vesicles are empty or filled and the nature of the filling.
7. Color name and code (for the dry rock surface) according to the Munsell rock color charts (Rock-Color Chart Committee, 1991).
8. Structure. This entry refers to whether the unit is massive, pillowed, hyaloclastic, banded, brecciated, scoriaceous, or tuffaceous.
9. Alteration. We graded the degree of alteration as unaltered (F; <2% of alteration products by volume); slight (S; 2%–<10%); moderate (M; 10%–<40%); high (H; 40%–<80%); very high (VH; 80%–<95%); or complete (C; 95%–100%). Changes of alteration through a section or a unit were also noted.
10. Veins and fractures: their abundance, width, and mineral linings and fillings.
11. Any additional comments.

Thin Section Description of Igneous Rocks

We examined thin sections from the core intervals noted on the VCD forms to complement and refine the hand specimen observations. In general, the same terminology was used for thin section descriptions as for the visual core descriptions. The percentages of individual phenocryst, groundmass, and alteration phases were estimated visually, and textural descriptions are reported in table format. The textural terms used are defined by MacKenzie et al. (1982). Thin section exami-

nation resulted in modification of some rock names. At least one thin section per subunit was described.

X-Ray Diffraction

Selected samples were taken for qualitative mineral analysis with an XRD Philips model PW1729 X-ray diffractometer using Ni-filtered CuK_α radiation. Instrument conditions were as follows: 40 kV, 35mA; goniometer scan from 2° to 70°2θ (air-dried samples) and from 2° to 12°2θ (glycolated samples); step size of 0.01°2θ; scan speed at 1.2°2θ/min; and count time of 0.5 s for each step.

Some samples were decalcified using 10% acetic acid then washed repeatedly with demineralized water in a centrifuge. The carbonate-free fraction was deflocculated with a 1% Calgon (sodium hexametaphosphate) solution and homogenized in a sonic dismembrator for 1 min. The clay fraction (<2 µm) was then separated by centrifugation, and the clay residue was deposited onto glass slides. MacDiff software (version 4.1.1 PPC by Rainer Petschick) was used to display diffractograms, and identifications are based on multiple peak matches, using the mineral database provided with MacDiff. Diffractograms were peak corrected to match the calcite peak at 3.035 Å. In the absence of calcite, no peak correction was applied.

Digital Color Imaging

A digital core imaging system (DIS) was installed during the port call prior to Leg 198. For the first time, systematic, high-resolution digital scanning of the archive half of each core was included in the shipboard core flow (following core description). The images for each core section are available in the Janus database (see the **"Related Leg Data"** contents list).

BIOSTRATIGRAPHY

Preliminary age assignments were primarily based on biostratigraphic analyses of calcareous nannofossils and planktonic foraminifers. Paleodepth interpretations were based on benthic foraminifers. Calcareous nannofossil and planktonic foraminiferal datums were determined by examining core catcher samples. Additional samples were examined in order to refine the biostratigraphy of both groups where appropriate and to discern unconformities and other critical intervals. The preservation, abundance, and zonal assignment for each sample and for each microfossil group were recorded in the stratigraphic site summary sheets and entered into the Janus database. The timescale of Berggren et al. (1995b) was applied for the Cenozoic and those of Gradstein et al. (1995) and Channell et al. (1995) for the Cretaceous (Figs. **F4, F5**).

Calcareous Microfossil Datums

Ages of Cenozoic calcareous nannofossil and planktonic foraminiferal first and last occurrences (FO = first occurrence or datum base, LO = last occurrence or datum top) older than 14 Ma follow Berggren et al. (1995b); younger datums are astrochronologically tuned ages from several sources (Shackleton et al., 1995; Backman and Raffi, 1997; Chaisson

F4. Timescale and primary calcareous microfossil datums, Cenozoic and Cretaceous, p. 45.

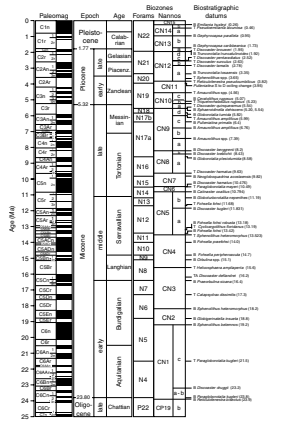

F5. Timescale and primary calcareous and siliceous microfossil datums, Late Jurassic–Early Cretaceous, p. 50.

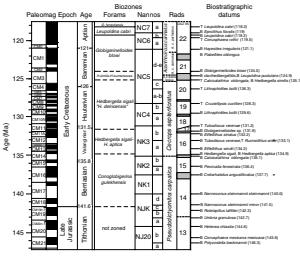

and Pearson, 1997). Ages for Cenozoic datums are presented in Tables T1 and T2. Age estimates for Cretaceous calcareous nannofossil and planktonic foraminiferal datums are from Erba et al. (1995), Bralower et al. (1997), and Premoli Silva and Sliter (1999). Cretaceous datums are presented in Tables T3 and T4.

T1. Cenozoic calcareous nannofossil datums, p. 54.

T2. Cenozoic planktonic foraminiferal datums, p. 56.

T3. Cretaceous calcareous nannofossil datums, p. 58.

T4. Cretaceous planktonic foraminiferal datums, p. 59.

Calcareous Nannofossil Zonal Scheme and Taxonomy

The zonal scheme of Bukry (1973, 1975; zonal code numbers CN and CP added and modified by Okada and Bukry, 1980) was used for Cenozoic calcareous nannofossil biostratigraphy (Table T1). The zonal schemes of Sissingh (1977; CC zones), as modified by Perch-Nielsen (1985), and Burnett (1999; UC zones) were used for the Late Cretaceous, and those of Roth (1978, 1983; NC zones) with subdivisions by Bralower et al. (1993) were used for the Early Cretaceous (Table T3). The zonal scheme of Bralower et al. (1989; NK and NJK zones) was applied for the Jurassic/Cretaceous boundary interval. All of these zonations represent a general framework for the biostratigraphic classification of mid- to low-latitude nannofloral assemblages and are presented in Figures F4 and F5. Nannofossil taxonomy follows that used in Bown (1999), where full taxonomic lists can be found.

Planktonic Foraminiferal Zonal Scheme and Taxonomy

The tropical planktonic foraminiferal zonal scheme (N and P zones) used for the Cenozoic follows Berggren et al. (1995b; Table T2). The zonation used for Cretaceous planktonic foraminifers is based on the tropical zonal schemes of Caron (1985) and Sliter (1989; KS zones) with modifications by Bralower et al. (1993, 1995, 1997) and by Premoli Silva and Sliter (1994, 1999) (Figs. F4, F5). Age estimates for planktonic foraminiferal datum markers were obtained from Erba et al. (1995), Bralower et al. (1997), and Premoli Silva and Sliter (1999; Table T4).

Cenozoic taxonomic concepts follow Postuma (1971), Kennett and Srinivasan (1983), Bolli and Saunders (1985), Toumarkine and Luterbacher (1985), Spezzaferri and Premoli Silva (1991), Chaisson and Leckie (1993), Leckie et al. (1993), Spezzaferri (1994), Pearson (1995), Berggren and Norris (1997), Chaisson and Pearson (1997), Pearson and Chaisson (1997), Norris (1998), and Olsson et al. (1999). Genus-species combinations generally follow those used by Berggren et al. (1995b) with few modifications. Cretaceous taxonomic concepts are based on Longoria (1974), Robaszynski et al. (1979, 1984), Leckie (1984), Caron (1985), Nederbragt (1990, 1991), and Petrizzo (2000).

Benthic Foraminiferal Taxonomy and Paleodepth Determination

At suprageneric levels, the classification scheme of Loeblich and Tappan (1988) is followed here, with the exception of trochospirally coiled calcareous taxa, which are classified according to the scheme of Kaiho (1998). Cenozoic benthic foraminiferal taxonomic concepts were mainly based on Tjalsma and Lohmann (1983), van Morkhoven et al. (1986), Kaiho (1992), and Bolli et al. (1994). Cretaceous taxonomic concepts follow Luterbacher (1973), Sliter (1977, 1980), Gradstein (1978), Bolli et al. (1994), Holbourn and Kaminski (1997), and Kaiho (1998).

Neogene paleodepth estimates are based on the work of Pflum and Frerichs (1976), Woodruff (1985), and van Morkhoven et al. (1986). For

the Cretaceous section, estimates are mainly based on the studies of Sliter (1977, 1980) Nyong and Olsson (1984), Kaiho (1998), Holbourn et al. (2001), and a backtracked paleodepth curve from Deep Sea Drilling Project (DSDP) and ODP data of Kaiho (1999). The following terminology was applied:

Neritic = 0–200 m.
Upper bathyal = 200–500 m.
Middle bathyal = 500–1000 m.
Lower bathyal = 1000–2000 m.
Upper abyssal = 2000–3000 m.
Lower abyssal = 3000–4000 m.

Early Cretaceous Radiolarian Zonal Scheme and Taxonomy

The taxonomy of Early Cretaceous radiolarians is based on Baumgartner et al. (1995b). Eleven radiolarian Unitary Association Zones (UAZs) characterize the uppermost Jurassic and Lower Cretaceous interval and can be used for biostratigraphic correlation (Baumgartner et al., 1995a). A UAZ is a "maximal set of mutually compatible taxa" (Baumgartner et al., 1995a, p. 1014). The age correlation of radiolarian UAZs in the upper Barremian to Aptian interval follows Erba et al. (1999), and the uppermost Jurassic–lower Barremian interval is correlated to the Mesozoic polarity chronozones (Gradstein et al., 1995) by Baumgartner et al. (1995a).

Methods of Study for Calcareous Nannofossils

Calcareous nannofossils were examined in smear slides using standard light microscope techniques, under crossed polarized light, transmitted light and phase contrast at 1000× magnification. The following abbreviations were used to describe nannofossil preservation:

VG = very good preservation (no evidence of dissolution and/or recrystallization, no alteration of primary morphological characteristics and specimens identifiable to the species level).
G = good preservation (little or no evidence of dissolution and/or recrystallization, primary morphological characteristics only slightly altered, and specimens identifiable to the species level).
M = moderate preservation (some etching and/or recrystallization, primary morphological characteristics somewhat altered, and most specimens identifiable to the species level).
P = poor preservation (severely etched or overgrown, primary morphological characteristics largely destroyed, fragmentation has occurred, and specimens often unidentifiable at the species and/or generic level).

Six calcareous nannofossil abundance levels are recorded as follows:

D = dominant (>100 specimens per field of view).
A = abundant (>10–100 specimens per field of view).
C = common (1–10 specimens per field of view).
F = frequent (1 specimen per 1–10 fields of view).

R = rare (<1 specimen per 10 fields of view).
B = barren.

Methods of Study for Foraminifers

Foraminifers from unlithified ooze were soaked in a 3% solution of hydrogen peroxide with a small amount of Calgon added and then washed with tap water over a 63-µm sieve (Quarternary–lower Eocene interval) or a 45-µm sieve (basal Eocene–Upper Cretaceous interval). Semilithified ooze and chalk were first partially fragmented by hand and then soaked in hydrogen peroxide and Calgon before washing. After every use, the sieve was dipped in a dilute solution of methyl blue dye to identify contaminants from previous samples. After washing, all samples were collected on filter paper and then dried on a hot plate at ~50°C.

Species identification for planktonic foraminifers were generally made on the >250-µm and >150-µm size fractions. Two picking trays per sample from >250-µm size fraction (Neogene) or the >125-µm fraction (Paleogene–mid-Cretaceous) were examined for identification and abundance estimation of benthic foraminifers. Samples within 0.5 m above the Cretaceous/Tertiary (K/T) boundary and the Lower Cretaceous were treated the same as other unlithified ooze samples except that a 38-µm sieve was used to isolate the dwarfed microfossil assemblages.

The following abundance categories were estimated from visual examination of the dried sample for planktonic foraminifers:

D = dominant (>30%).
A = abundant (>10%–30%).
F = few (>5%–10%).
R = rare (1%–5%).
P = present (<1%).

The following abundance categories were used for benthic foraminiferal abundance (as a group) based on the number of benthic foraminifers encountered in two picking trays:

A = abundant (>100 specimens).
C = common (>50–100 specimens).
F = few (>20–50 specimens).
R = rare (10–20 specimens).
T = trace (<10 specimens).

The preservation of the planktonic and benthic foraminifers was estimated as follows:

VG (very good) = no evidence of overgrowth, dissolution, or abrasion.
G (good) = little evidence of overgrowth, dissolution, or abrasion.
M (moderate) = moderate calcite overgrowth, dissolution, or abrasion.
P (poor) = substantial overgrowth, dissolution, or fragmentation.

Methods of Study for Lower Cretaceous Radiolarians

Radiolarians were extracted from claystone, chalk, and porcellanite by applying the same preparation method used for foraminifers, and they were studied in the stereomicroscope.

PALEOMAGNETISM

Paleomagnetic investigations aboard the *JOIDES Resolution* during Leg 198 were mainly of two types: routine measurements of the natural remanent magnetization (NRM) of archive-half core sections, before and after alternating-field (AF) demagnetization, and low-field magnetic susceptibility (k) measurements. Discrete samples were collected during the cruise from working halves of core sections in standard (7 cm^3) plastic "cubes" with the orientation arrow on the sample pointing upcore. The sampling frequency was generally three samples per section from one hole per site and one or two samples per section from duplicate holes. Intervals of drilling-related core deformation were obviously avoided, where apparent. Apart from a few test samples, remanence measurements of discrete samples were not taken because sediment sample magnetizations are too weak to be measured reliably with shipboard equipment. The discrete samples will be analyzed on shore with three objectives: (1) to ground truth the shipboard polarity stratigraphies, (2) to gain insight into the magnetic properties of the sediments and determine the mineralogy and grain size of remanence carriers, and (3) to determine paleolatitudes for tectonic studies.

The remanent magnetization of archive halves of core sections was measured using the shipboard 2-G Enterprises (model 760R) long-core cryogenic magnetometer. This instrument is equipped with direct-current super-conducting quantum interference devices (DC SQUIDs) and has an in-line, automated AF demagnetization system. The pick-up coils of the cryogenic magnetometer measure the core over a width of a little more than 30 cm, although ~85% of the remanence is sensed from a 20-cm width. Because of this window size and the 5-cm sampling interval, adjacent measurements made on Leg 198 cores are not strictly independent. A background resolution limit is imposed on the measurement of sample remanence by the magnetization of the core liner itself, which is ~3×10^{-5} A/m. The standard ODP magnetic coordinate system was used (+x: vertical upward from the split surface of archive halves, +y: left along split surface when looking upcore, and +z: downcore; see Fig. **F6**).

NRM was routinely measured on all archive-half sections at 5-cm intervals, starting 20 cm above the core section top and 20 cm below the core section base. The large leader and trailer distance (20 cm) allows future deconvolution of the core data. For shipboard analyses, measurements within 10 cm from the ends of each section were disregarded because of end effects. After measurement of the NRM, AF demagnetization was routinely applied using peak fields of 5, 10, and 20 mT. The maximum peak field (20 mT) was set at this low level to prevent compromising the archive halves of core sections for further (shore based) studies. Specifically, we plan postcruise sampling of archive halves of core sections using u-channels to resolve the magnetic stratigraphy (including paleointensity stratigraphy) at a resolution beyond the limits of the shipboard magnetometer.

During APC coring, full orientation was attempted using the Tensor Multishot Tool, which is rigidly mounted onto a nonmagnetic sinker bar, attached to the top of the core barrel assembly. The Tensor Tool consists of three mutually perpendicular magnetic field sensors and two perpendicular gravity sensors. The information from both sets of sensors allows the azimuth and dip of the hole to be measured, as well as

F6. ODP magnetic orientation convention, p. 51.

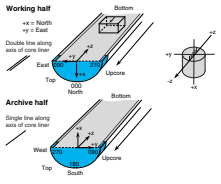

the azimuth of the APC core (the azimuthal reference line is the double orientation line on the core liner).

Where magnetic cleaning appears, from shipboard data, to have isolated the characteristic remanent magnetization, paleomagnetic inclinations were used to make an initial designation of magnetic polarity zones. The geomagnetic polarity timescale (GPTS) of Cande and Kent (1995) provides the polarity zone template for the Late Cretaceous and Cenozoic. Biostratigraphic constraints should allow us to correlate polarity zones to the GPTS and, hence, to assign initial ages to the sedimentary sequence. For Early Cretaceous polarity intervals prior to the Cretaceous Long Normal Superchron, the GPTS of Channell et al. (1995) was used as the polarity zone template and to provide ages of polarity chrons.

Although the great majority of Leg 198 paleomagnetic measurements were of sedimentary cores, a few were made on igneous rocks cored in Hole 1213B. As for sediment core measurements, the igneous cores were measured at 5-cm intervals. Only sections with long, whole pieces were measured, but because of piece breakage and some small pieces, some measurements are spurious. For interpretation, only the measurements located in the interior zones of the long pieces were used. AF demagnetization was used to remove low coercivity overprints, with the usual steps (10, 15, and 20 mT) augmented up to 30–35 mT.

Magnetic susceptibility was measured for each whole-core section as part of the MST analysis (see **"Physical Properties,"** p. 22). Susceptibility is measured on the MST using a Bartington MS2 meter coupled to a MS2C sensor coil, with a diameter of 8.8 cm operating at 0.565 kHz. The sensor was set on SI units, and the data were stored in the Janus database in raw meter units. The sensor coil is sensitive over an interval of ~4 cm (half-power width of the response curve), and the width of the sensing region corresponds to a volume of 166 cm^3 of cored material. To convert to true SI volume susceptibilities, these values should be multiplied by 10^{-5} and then multiplied by a correction factor to account for the actual volume of material that passed through the susceptibility coils. Except for measurements near the ends of each section, the correction factor for a standard full ODP core is ~0.68. The end effect of each core section is not adequately corrected using this procedure.

COMPOSITE DEPTHS

The recovery of complete sediment sections of APC-cored intervals was crucial to the paleoceanographic objectives of Leg 198. Drilling of parallel holes at Sites 1209 through 1212 ensured that intervals missing from one APC hole as a result of recovery gaps between cores were recovered in an adjacent hole. During Leg 198, continuity of recovery was confirmed by composite depth sections developed for all multiple-cored sites. Adjustments to the shipboard mbsf depth scale are required for several reasons (Ruddiman et al., 1987; Farrell and Janecek, 1991; Hagelberg et al., 1992; Hagelberg et al., 1995). Rebound of the sediment following core recovery causes the cored sediment sequence to be expanded relative to the drilled interval. In addition, random variations in ship motion and heave can affect the true in situ depth of each core. Portions of the sediment sequence are usually missing in section breaks, even between successive cores having ≥100% recovery. As a result, the composite depth scale grows downhole relative to the mbsf scale, typically on the order of 10%. (e.g., Lyle, Koizumi, Richter, et al., 1997;

Hagelberg et al., 1995; Alexandrovich and Hays, 1989; Farrell and Janecek, 1991; Acton et al., 2001; J. McGuire and G.D. Acton, unpubl. data).

A composite depth scale places coeval, laterally continuous stratigraphic features into a common frame of reference by shifting the mbsf depth scales of individual cores to maximize the correlation between holes (Sacks, Suyehiro, Acton, et al., 2000). The individual cores are shifted vertically without permitting expansion or contraction of the relative depth scale within any core. Deviations of mbsf depths from true depths arise from factors such as uncertainties in depth measurements (most of which can be attributed to ship motion), core expansion, and incomplete recovery. Therefore, a horizontal feature present in recovered material from several holes will have, in the absence of local bathymetric variations, the same true depth but will likely have different mbsf depths. Errors in the mbsf depth scale range from a few centimeters to several meters, though rarely more than ~10 m (e.g., Acton et al., 2001, and references therein). After establishing a meters composite depth (mcd) scale, more complete stratigraphic records are spliced from the data from multiple holes.

The methods used during Leg 198 were similar to those used to construct composite depth sections during Legs 138 (Hagelberg et al., 1992), 154 (Curry, Shackleton, Richter, et al., 1995), 162 (Jansen, Raymo, Blum, et al., 1996), 167 (Lyle, Koizumi, Richter, et al., 1997), 178, (Acton et al., 2001), 186 (J. McGuire and G.D. Acton, unpubl. data), and 189 (Exon, Kennett, Malone, et al., 2001). At each site, closely spaced (2.5- or 3-cm interval) measurements of magnetic susceptibility and gamma ray attenuation (GRA) bulk density were made on the MST soon after the core sections had equilibrated to room temperature. The susceptibility values are presented as raw meter values, which can be converted to SI volume susceptibility units by multiplying by ~0.68×10^{-5} (Blum, 1997). These measurements were entered into the shipboard Janus database. In addition, measurements of spectral reflectance were made at 2.5 cm resolution on the split cores (see **"Lithostratigraphy,"** p. 4). Magnetic susceptibility values, total reflectance (L*) values from the spectral reflectance measurements, and GRA bulk density measurements from each hole were compared to determine if coring offsets were maintained between holes. Integration of at least two different physical properties allowed more reliable hole-to-hole correlations than would be possible with a single data set. In addition, magnetic susceptibility data collected from intervals that were disturbed by the drilling and recovery process were removed before making correlations for the mcd scale. This includes gaps caused by the removal of 5-cm-long interstitial water (IW) samples, which are taken from the ends of some sections prior to MST and other measurements.

The mcd scale was constructed using the program SPLICER (version 2.2, available on the Internet from Lamont-Doherty Earth Observatory Borehole Research Group [LDEO-BRG] at **http://www.ldeo.columbia.edu/BRG/ODP**). SPLICER allows data sets from several holes at a given site to be correlated simultaneously. Corresponding features in data sets from adjacent holes were aligned based on graphical and mathematical cross-correlations using an iterative process. Features were aligned by adjusting the ODP coring depths in mbsf, measured from the length of the drill string advanced, on a core-by-core basis. No depth adjustments were made within an individual core. Correlations were first made visually by selecting a tie point from data in one hole and comparing it di-

rectly with data from another hole. Ties are intended to correlate data based on matching patterns and amplitudes of the data sets.

Cross-correlation coefficients for all data sets were calculated within SPLICER. Depth adjustments were chosen that provided the best correlation within a preferred data set or the best compromise of correlation coefficients among all the data sets. The values of the cross-correlation coefficient vary from +1 to –1, with +1 indicating perfect correlation (such as would be obtained by comparing identical data sets) and –1 indicating anticorrelation (such as would be obtained by comparing a data set to its inverse). Values near zero indicate poor or no correlation. Each time a depth adjustment is made within SPLICER, the coefficient is recalculated, allowing the user to determine the preferred correlation. The window over which the coefficient is calculated is adjustable. The default window length of ±2.00 m on either side of the selected tie point was used for most correlations. This window was reduced to ±1.00 m as needed to focus on features of interest or to avoid spurious features such as those biased by coring disturbances.

Correlation began by selecting the core that had the most pristine record of the upper portion of the upper few meters of the sedimentary record, particularly the mudline. This first core is defined as the top of the composite section, and its mcd depth is the same as its mbsf depth. At Site 1209, the top of the composite section was Core 198-1209A-1H. A tie point that gives the preferred correlation was selected between data from this core and a core in a second hole. All of the data from the second hole below the correlation point were vertically shifted to align the tie points between the holes. Once the appropriate tie was determined and the depth adjustment was made, the shifted section became the reference section, and a tie was made to a core from the first hole. The process continued downhole, vertically shifting the data one core at a time, relative to data from the other hole. By tying points of different mbsf depths, SPLICER vertically adjusted the individual sections of the cores and brought the chosen anomalies into the common mcd depth scale. The tie points were added to the SPLICER "affine" table, which records all of the depth adjustments that define the composite depth scale, in mcd.

The composite depth section for each site is presented in tabular form in the "Composite Depths" section of each site chapter. The composite depth table of Site 1209 is given as an example in Table **T5.** For each core, the depth adjustment required to convert from the mbsf depth scale to the mcd scale is given. The last two columns in each table give, for each core, the cumulative-depth offset added to the ODP curatorial subbottom depth (in mbsf) and the composite depth (in mcd), respectively. The depth-offset column facilitates conversion of sample depths that are recorded in ODP curatorial subbottom depth (in mbsf) to composite depth (in mcd). The equivalent depth in mcd is obtained by adding the amount of offset listed to the depth in mbsf of a sample taken in a particular core.

The need for a composite section to verify stratigraphic continuity is illustrated in Figure **F7.** In the leftmost panel, magnetic susceptibility data from three holes at Site 1211 are shown on the mbsf depth scale. In the middle panel, the same records are shown after depth scale adjustment so that correlative features are aligned. The correlation of lithologic parameters between parallel holes and associated depth adjustments for individual cores was optimized in such a way that a single record could be sampled from the aligned cores without any additional depth scale changes. The right panel shows the resulting spliced record.

T5. Example from Site 1209 of a composite depth table, p. 60.

F7. Magnetic susceptibility data from three holes at Site 1211, with depth scale adjustment and resulting splice record, p. 52.

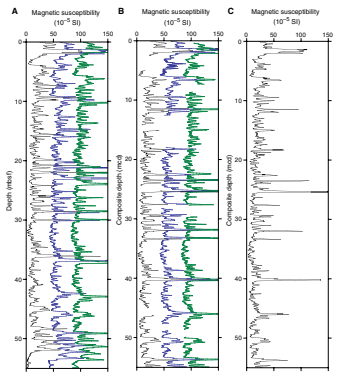

Where the amount of offset necessary to align features was ambiguous or imprecise for all lithologic parameters or where multiple hole data were unavailable (e.g., for the sediments below the uppermost Maastrichtian), no additional depth adjustments were made. In these cases, the total amount of offset between mbsf depth and mcd is equal to the cumulative offset from the overlying cores. The composite depth section extends to the base of the core including the K/T boundary interval.

For each site, after the composite section was constructed, a representative spliced record was assembled. Because the missing intervals between successive cores in the sedimentary sequence could be identified, it was possible to splice in these missing intervals with data from adjacent holes. The resulting composite record ("splice") provides a single representative record of each lithologic parameter (i.e., magnetic susceptibility, spectral reflectance, and GRA bulk density) for a given site. Additionally, these records are ideally suited for serving as sampling schemes for paleoceanographic studies.

Splice tie points were made between adjacent holes at identifiable, highly correlated features. Each splice was constructed beginning at the mudline at the top of the composite section and working downward. Typically, one hole is chosen as the backbone for the record, and cores from other holes are used to patch in the missing intervals in the core gaps (Fig. F7). Intervals were chosen for the splice so that section continuity was maintained, whereas disturbed intervals were avoided.

Tables that give the tie points for construction of the spliced records are presented in each site chapter. By identifying intervals where features present in the multiple-cored holes were most highly correlated, it was possible to construct a spliced record that avoided duplication or omission of individual features or cycles. Splice tie points always connect features with exactly the same composite depths. As a result, the final alignment of the adjacent holes could be slightly different from the best overall visual or quantitative hole-to-hole correlation. Further adjustments to the composite depth section by expanding and compressing the depth scale within individual core intervals are required to align all features exactly. These additional adjustments will be made as part of normal postcruise studies.

SEDIMENTATION AND ACCUMULATION RATES

To determine sedimentation rates, one must first generate an age-depth relationship. At a site with precisely determined paleomagnetic stratigraphy and with unambiguously identified chrons, accumulation rate uncertainties arise almost entirely from uncertainties in the ages of reversal boundaries.

Where biostratigraphic datums are used, the chief uncertainty arises from the fact that, with a limited amount of time for study, many datums are determined among widely separated samples. During many ODP legs, it has been necessary to reconstruct sedimentation rates using datums determined only in core catchers (i.e., within 9.5 m). The amount of uncertainty in each sedimentation rate estimate derived in this way is related to the thickness interval over which it is averaged, divided by the combined uncertainty in the top and bottom controls.

The second source of uncertainty in sedimentation rates is the age of the datums, which of course increases as the uncertainty in the datum ages increases. Our aim is to use a prime set of datums, distributed less

than 2 m.y. apart, and to determine these datums in all sites to within one section (1.5 m) or better.

Sedimentation rates (in meters per million years) were estimated from age-depth plots by drawing best-fit lines through all the biostratigraphic or paleomagnetic data over successive depth intervals (i.e., by drawing straight-line segments through discrete intervals of data). All sedimentation rates were calculated using midpoints in the observed depth uncertainty range. In reality, each datum event has an age uncertainty that may vary from a few thousand years to a few hundred thousand years. At a sedimentation rate of 20 m/m.y., datums spaced at 9.5-m intervals would only allow breaking the accumulation rates into roughly 4-m.y. increments, if we aim for an uncertainty better than ~±20%.

Bulk sediment mass accumulation rates (MARs) (in grams per square centimeter per thousand years) are calculated from linear sedimentation segments and dry bulk density data (grams of dry sediment per wet volume; in grams per cubic centimeter) (see **"Index Properties,"** p. 24, in "Physical Properties"). Only those samples with both dry bulk density and nearby carbonate data (within 4 cm) were used to calculate MARs for the carbonate and noncarbonate fractions. Carbonate MARs were calculated by multiplying bulk sediment MARs by percent carbonate, whereas the noncarbonate MARs represent the difference between bulk and carbonate MARs. Ages were interpolated for all samples based on the linear sedimentation rate segments. Higher-frequency variations in percentage of carbonate obviously imply that higher-frequency variations in accumulation of either carbonate or noncarbonate are superimposed on relatively stable long-term accumulation rates. Variable preservation of the carbonate fraction may also play a role.

ORGANIC GEOCHEMISTRY

The shipboard organic geochemistry program for Leg 198 included (1) real-time monitoring of volatile hydrocarbons (HC) in headspace gases as required by ODP safety regulations; (2) measurement of inorganic carbon (IC) and carbonate content of the sediments; (3) elemental analyses of total carbon, nitrogen, and sulfur; (4) characterization of organic matter (OM) by Rock-Eval pyrolysis; and (5) examination of composition of solvent-extractable components.

The laboratory methodologies and instruments employed during Leg 198 follow those used in recent ODP legs, as described in the "Explanatory Notes" chapters and supplemented by the technical guides for shipboard organic geochemistry (Emeis and Kvenvolden, 1986; Kvenvolden and McDonald, 1986; Pimmel and Claypool, 2001).

Volatile Hydrocarbons

Concentrations of light hydrocarbon gases methane (C_1), ethane (C_2), and propane (C_3) were monitored for safety and pollution prevention. The C_1/C_2 ratio obtained is particularly important for indicating potential petroleum occurrences; sediments rich in organic carbon (C_{org}) commonly have a ratio of >1000, whereas values <200 may indicate potential petroleum generation related to increasing depth and temperature (cf. Stein et al., 1995).

Sampling of headspace gases in each core followed the standard procedure described by Kvenvolden and McDonald (1986). Immediately af-

ter core retrieval on deck, an ~5-cm³ sediment sample was collected using a borer tool, placed in a 21.5-cm³ glass serum vial, and sealed on deck or immediately in the lab with a septum and metal crimp cap. For consolidated or lithified samples, chips of material were placed in the vial and sealed. Prior to gas analyses, the vial was heated at 70°C for a minimum of 20 min. A 5-cm³ subsample of the headspace gas was extracted from each vial using a 5-cm³ glass gas syringe and analyzed by gas chromatography (GC).

Gas HC constituents were analyzed using a HP5890 II gas chromatograph equipped with a sample loop, an 8 ft × 1/8 in stainless-steel column packed with HayeSep R, and a flame ionization detector (FID). Helium was used as a carrier gas. HP Chemstation software was used for data acquisition and processing. Chromatographic responses were calibrated using commercial standards (Scotty II Analyzed Gases, Scott Specialty Gas Co.) and the results reported in parts per million by volume (ppmv [µL/L]).

Headspace sampling is an important but rather inconsistent procedure for shipboard analysis of hydrocarbon gases. Sample size and nature can vary, depending on the condition of the core. This can range from soft, organic-rich clay, when the borer tool can be employed, to hard carbonate-rich sediment, from which sample pieces must be cut. Higher C_1, C_2, and C_3 values per gram of sediment were generally obtained from coherent cylindrical samples taken by the cork borer than from discrete pieces of lithified sediment. This discrepancy may also reflect the inherent capacity of the sediment lithology to retain hydrocarbons, but it appears not to affect the C_1/C_2 ratio. It is clearly important to employ consistent sample-collection procedures for comparable downcore headspace hydrocarbon analysis. Additional gas may be released by further heating if necessary for replicate analyses of the same headspace sample. Reheated samples generally yield 10%–50% lower C_1–C_3 absolute abundances, but the C_1/C_2 ratios appear to be unaffected. Therefore, this may be a viable method for verifying anomalous C_1/C_2 values of sediments.

Carbonate Analysis

The percentage of IC was determined using a Coulometrics 5011 CO_2 coulometer equipped with a System 140 carbonate analyzer. A total of ~10–12 mg of freeze-dried, ground sediment was reacted with 2 N HCl to liberate CO_2. The change in light transmittance monitored by a photodetection cell controlled the CO_2 titration. The percentage of carbonate was calculated from the IC content using the following equation:

$$CaCO_3\ (wt\%) = IC\ (wt\%) \times 8.33.$$

This method assumes that all of the CO_2 evolved was derived from dissolution of calcium carbonate. No corrections were made for other carbonate minerals.

Elemental Analysis

Total carbon (TC), nitrogen, and sulfur were determined using a Carlo Erba 1500 CNS analyzer, which combusts sediment samples in tin cups with an oxidant (V_2O_5) at 1000°C in a stream of oxygen. Nitrogen oxides were reduced to N_2, and the mixture of N_2, CO_2, H_2O, and SO_2 gases was separated by gas chromatography and detection performed by

a thermal conductivity detector (TCD). The H_2 value is not useful because it represents hydrogen derived from OM as well as water bound to clay minerals.

The analytical procedure employed a new combustion column for each sample batch. An aliquot of 5–15 mg freeze-dried, crushed sediment with ~10 mg V_2O_5 oxidant was combusted at 1000°C in a stream of oxygen. All measurements were calibrated by comparison to pure sulfanilamide as standard. The amount of total organic carbon (TOC) was calculated as the difference between TC and IC (determined from coulometry):

$$\text{TOC (wt\%)} = \text{TC (wt\%)} - \text{IC (wt\%)}.$$

In addition to the carbon analytical data, the C/N atomic ratio can be used to identify the source of the organic matter (fresh marine C/N: 6 to 8, degraded marine C/N: 8 to 20, and terrestrial C/N: >25). However, extensive diagenesis and burial can also increase the C/N ratio of marine OM to 15 or greater (Meyers, 1994), and/or the C/N ratio can be lowered by oxidation of organic carbon and sorption of ammonia on clay minerals (e.g., Müller, 1977).

Organic Matter Characterization and Maturity Determination

The type of organic matter was characterized by programmed pyrolysis using a Delsi Rock-Eval II system. This method is based on a whole-rock pyrolysis technique designed to identify the type of OM and its maturity and to evaluate the petroleum potential of sediments (Espitalié et al., 1986), while also providing a measure of TOC.

The Rock-Eval system includes a temperature program that first releases volatile hydrocarbons (S_1) at 300°C for 3 min. Hydrocarbons are then released via thermal cracking of kerogen (S_2) as the temperature is increased to 550°C at 25°C/min. The S_1 and S_2 hydrocarbons are measured by FID and reported in milligrams per gram of dry sediment. The temperature at which the kerogen yields the maximum amount of HC (top of the S_2 peak) provides the parameter T_{max}, used to assess the maturity of the OM. Between 300° and 390°C of the programmed pyrolysis, CO_2 released from the thermal degradation of organic matter (S_3) is trapped and subsequently measured by a TCD and reported in milligrams per gram dry sediment. Rock-Eval parameters facilitate characterization of OM by allowing the following indices to be calculated: hydrogen index (HI = S_2/TOC × 100), oxygen index (OI = S_3/TOC × 100), and S_2/S_3 ratio. In general, high OI values (>100) are an indicator of terrestrial OM or of immature OM of all sources. The production index is defined as $S_1/(S_1+S_2)$. This value is usually <0.2 in immature rocks; values of 0.3 to 0.4 are typical for samples in the petroleum window (T_{max} = 420–450°C). Values of >0.5 may indicate the proximity of migrated HC or trapped petroleum. Interpretation of Rock-Eval OI data is compromised for samples containing >10 wt% carbonate, and the values themselves are also unreliable for young and immature OM (<1 Ma or T_{max} < 400°C). Samples with <0.5 wt% TOC may not give reliable results because of the small size of the S_1, S_2, and S_3 signals.

Solvent Extractable Component: Higher Hydrocarbons and Ketones

Solvent-extractable organic constituents were examined to assess the characteristics of organic matter in Cretaceous black shales, especially the origin of the organic matter. The focus of these analyses were qualitative—to recognize the identity of the hydrocarbons and other components present and their relative abundance. No quantitative determination of the concentrations of individual constituents was made.

Extraction procedures were as follows: ~1–4 g of sediment were extracted ultrasonically using CH_2Cl_2 (8 mL) for 30 min. The extract was transferred to a vial and reduced to dryness under N_2. It was transferred in hexane to a silica column to remove polar constituents and recover hydrocarbon and ketone fractions by successive elution with hexane (4 mL) and CH_2Cl_2 (4 mL). Each eluant was taken to near dryness under N_2 and transferred using hexane (50–100 µL) to a vial (with small-volume insert) for analysis by gas chromatography–mass selective detector (GC-MSD). An extraction of 1 g of Colorado oil shale was used to test these procedures. The hexane eluate is predominantly aliphatic hydrocarbons and less-polar aromatic hydrocarbons (e.g., monoaromatics). The CH_2Cl_2 eluate contains aromatic hydrocarbons and ketones, including alkenones.

The GC-MSD is a Hewlett-Packard 6973 system consisting of a HP 6890 GC with an MSD and a HP 7683 automatic liquid sampler (ALS). The GC is equipped with an electronic program controlled (EPC) split-splitless injector and a HP capillary column (5% phenyl methyl siloxane; 30 m × 0.25 µm) programmed from 40° to 130°C at 20°C/min, then at 4°C/min to 320°C, and held isothermally at 320°C for 20 min. He is used as the carrier gas. The transfer line is set at 280°C, and the source of the MSD is set at 230°C. The MSD scanned from 27 to 500 m/z. HP MS Chemstation software was used for data acquisition and processing. The identity of individual hydrocarbons was determined from their mass spectral characteristics and GC retention times by comparison with the literature.

INORGANIC GEOCHEMISTRY

Interstitial Water Sampling and Chemistry

Shipboard interstitial water analyses were performed on 5- to 15-cm-long whole-round sections that were cut immediately after the core arrived on deck. In most cases, one whole-round section was taken from the lower third of each core. To avoid the destruction of critical intervals, whole-round sections were not removed from cores adjacent to such intervals as determined by shipboard biostratigraphy. Details of the sampling resolution are described in the individual site chapters of this volume. After extrusion from the core liner, the surface of each whole-round section was scraped with a spatula to remove potential contamination. Interstitial waters were collected using a titanium squeezer, modified after the standard ODP stainless steel squeezer of Manheim and Sayles (1974). Pressure up to 205 MPa (30,000 psi) was applied using a hydraulic press. Pore waters were passed through prewashed Whatman number 1 filters fitted above a titanium screen and subsequently extruded into a plastic syringe attached to the bottom of the squeezer assembly. All interstitial water samples were double-

filtered through 0.45-µm polycarbonate filters. Samples for shipboard analysis were stored in plastic vials pending analysis. Aliquots for future shore-based analyses were placed in glass ampules or plastic tubes and heat-sealed.

Interstitial water samples were routinely analyzed for salinity as total dissolved solids with a Goldberg optical handheld refractometer. The pH and alkalinity were determined by Gran titration with a Brinkmann pH electrode and a Metrohm autotitrator. Dissolved chloride was determined by titration with AgCl. Sodium (Na^+), potassium (K^+), magnesium (Mg^{2+}), calcium (Ca^{2+}), and sulfate (SO_4^{2-}) were analyzed by ion chromatography using a Dionex DX-120. Silica ($Si(OH)_4$), phosphate (HPO_4^{2-}), and ammonium (NH_4^+) concentrations were determined by spectrophotometric methods using a Milton Roy Spectronic 301 spectrophotometer (Gieskes et al., 1991). Iron (Fe^{2+}), manganese (Mn^{2+}), boron (H_3BO_3), lithium (Li^+), strontium (Sr^{2+}), and barium (Ba^{2+}) concentrations were determined by inductively coupled plasma–atomic emission spectroscopy (ICP-AES) following the general procedure outlined by Murray et al. (2000). In preparation for analysis by ICP-AES, aliquots of interstitial waters were acidified with nitric acid (HNO_3) and diluted tenfold with deionized (DI) water (0.5 mL of sample and 4.5 mL of DI water). Analytical blanks were prepared identically by analyzing DI water, which was acidified to matrix match the samples. At all sites, sodium was determined using charge balance calculations, where $S_{\text{cation charge}} = S_{\text{anion charge}}$. The chemical data for interstitial waters are reported in molar units. The reproducibility of results, determined via multiple determinations of International Association for the Physical Sciences of the Ocean standard seawater (alkalinity, Cl^-, Ca^{2+}, Mg^{2+}, K^+, and SO_4^{2-}), spiked surface seawater (ICP-AES determinations), or through the use of a calibration curve (NH_4^+, HPO_4^{2-}, and $Si(OH)_4$), is available in Table **T6.**

T6. Measured parameters, analytical methods, and reproducibility of results for interstitial water geochemistry, p. 61.

PHYSICAL PROPERTIES

Shipboard measurements of physical properties provide important information that assists in characterization of lithologic units, correlation of lithology with downhole geophysical logging data, assessment of the nature of consolidation, and interpretation of seismic reflection profiles. The primary objectives of the Leg 198 physical properties program were to collect high-resolution data to (1) facilitate hole-to-hole correlation and construction of composite stratigraphic sections, (2) allow correlation between sites, (3) enable postcruise cyclostratigraphy studies, (4) facilitate construction of synthetic seismic profiles, and (5) investigate the characteristics of major seismic reflectors.

Several types of physical properties measurements were initially performed on unsplit whole-round 1.5-m (and shorter) sections. Nondestructive measurements of wet bulk density, magnetic susceptibility, transverse compressional wave (*P*-wave) velocity and natural gamma radiation were made using the MST. The MST incorporates a GRA bulk density device, a *P*-wave logger (PWL), a magnetic susceptibility meter (MSM) and a natural gamma radiation (NGR) sensor. The quality of the MST data is highly dependent on the condition of the core. Thermal conductivity, using the needle-probe method, was measured at discrete intervals in whole-round sections. By comparison, discrete transverse compressional wave velocity and index properties measurements were

made on split-core sections. Index properties determined for discrete samples included wet bulk density, dry bulk density, grain density, water content, porosity, and void ratio. A comprehensive discussion of all methodologies and calculations used in the *JOIDES Resolution* physical properties laboratory can be found in Blum (1997).

MST Measurements

The principal aim of MST data acquisition during Leg 198 was to obtain high sampling resolution data sets, especially of GRA bulk density and magnetic susceptibility, to facilitate shipboard core-to-core correlation and the construction of composite stratigraphic sections. This objective had to be completed within a reasonable time frame without compromising the shipboard processing of recovered core. It should be noted that GRA, MSM, and PWL measurements are degraded in sections that contain gas voids, where the sediment does not fill the liner completely and where sediment is disturbed. Nevertheless, in such cases, the downhole data trends can still be useful for stratigraphic correlation.

The GRA bulk density device allows estimation of wet bulk density by measuring the attenuation of gamma rays that have passed through the cores, where the degree of attenuation is proportional to density (Boyce, 1976). Calibration of the GRA system was completed using known seawater/aluminum density standards. GRA bulk density data are of highest quality when determined on APC cores because the liner is generally completely filled with sediment. In XCB, MDCB, and RCB cores, however, GRA measurements are of lower quality and cannot be used to reliably determine bulk density on their own. The measurement width of the GRA sensor is ~5 mm, with sample spacing generally set at 3.0 cm (2.5 cm for Sites 1207 and 1208) for Leg 198 cores. The minimum integration time for a statistically significant GRA measurement is 1 s, and routine Leg 198 GRA measurements used either a 5- or 3-s integration time. A freshwater control was run with each section to measure instrument drift.

Whole-core magnetic susceptibility was measured with the MST using a Bartington MS2C meter with an 8-cm (internal diameter) loop. The measurement resolution of the MSM sensor is 4 cm, with a minimum statistically significant count time of 1 s. During Leg 198, MST magnetic susceptibility was routinely measured at a spacing of 3.0 cm (2.5 cm for Sites 1207 and 1208), with five data acquisitions. Magnetic susceptibility data were archived as raw instrument units and not corrected for changes in sediment volume, although a correction was made for instrument drift. To obtain SI units these raw instrument data need to be multiplied by 0.68×10^{-5} (Blum, 1997).

Transverse *P*-wave velocity was measured on the MST track with the PWL for all APC cores. The PWL was not used on XCB, MDCB, or RCB cores because the core liner/sediment interface is usually poor, resulting in poor acoustic coupling between the sediment and the liner and, thus, in inaccurate velocity determinations. The PWL transmits a 500-kHz compressional wave pulse through the core at 1 kHz. The transmitting and receiving transducers are aligned perpendicular to the core axis. A pair of displacement transducers monitors the separation between the compressional wave transducers so that variations in the outside diameter of the liner do not degrade the accuracy of the measured velocities. Calibration of the displacement transducer and measurement of electronic delay within the PWL circuitry were conducted us-

ing a series of acrylic blocks of known thickness and *P*-wave traveltime. Repeated measurement of *P*-wave velocity through a core liner filled with distilled water was used to check calibration validity. The measurement width of the PWL sensor is ~1 mm, with sample spacing routinely set at 2.5–10 cm for Leg 198 APC cores; analyses were completed in <1 s.

NGR was measured using the NGR sensor on the MST. The installation and operating principles of the NGR system used on the *JOIDES Resolution* are discussed by Hoppie et al. (1994). Data from 256 energy channels were collected and archived. For presentation purposes, the counts were summed over the range of 200–3000 keV, so as to be comparable with data collected during previous legs. This integration range also allows direct comparison with downhole logging data, which were collected over a similar integration range (Hoppie et al., 1994). Over the 200- to 3000-keV integration range, background counts, measured using a core liner filled with distilled water, averaged 30 during a 1-hr measurement period. Before taking measurements, each of the four NGR amplifiers were adjusted so that the thorium peak was at the highest resolution possible when the other three amplifiers were disabled. The multichannel analyzer was then calibrated by assigning certain channels to the characteristic energies of ^{40}K and the main peak of ^{232}Th (Blum, 1997). The measurement width of the NGR is ~15 cm, with a statistically significant count time of at least 5 s, depending on lithology. Because of the long time required for NGR measurements, sample spacing and count time for NGR measurements varied depending on the age and lithology of the sediment recovered. Natural gamma radiation data were not collected for all of the Leg 198 holes and sites. No corrections were made to NGR data obtained from XCB, MDCB, or RCB cores to account for sediment incompletely filling the core liner.

During Leg 198 activities some problems were encountered with the MST, GRA, and PWL sensors, resulting in significant and erroneous offsets in some data sets. These limitations to the Leg 198 MST-derived physical properties data are discussed in the relevant site chapters.

Index Properties

Index properties (wet and dry bulk density, grain density, water content, porosity, and void ratio) were determined from measurements of wet and dry sediment mass and dry sediment volume. Discrete samples of ~10 cm^3 were taken from soft sediments and placed in 10-mL beakers. One sample was routinely collected in each section of Hole A at each site and in each section of Holes B and C when these cored intervals were deeper than the base of Hole A.

Sample mass was determined with a reproducibility of ±3% standard deviation using a Scitech electronic balance. The balance was equipped with a computer averaging system that corrected for ship acceleration. The sample mass was counterbalanced by a known mass so that the mass differentials generally were <1 g. Sample volumes were determined using a Quantachrome Penta-Pycnometer, a helium-displacement pycnometer. Volume measurements were repeated at least three times, until the last two measurements exhibited <0.01% standard deviation. A reference volume was included within each sample set and rotated sequentially among the cells to check for instrument drift and systematic error. A purge time of 3–5 min was used before each run. The sample beakers used for discrete determination of moisture and density were calibrated before the cruise.

Individual index properties were calculated using measurements of wet and dry sediment mass and dry sediment volume; the latter two parameters were measured after samples had been oven dried at 105° ± 5°C for 24 hr and allowed to cool in a desiccator (see Blum, 1997, for relevant procedures and equations). This analytical method is preferred because volume measurements of wet samples are less accurate than dry volume samples. The procedures for the determination of these index properties comply with the American Society for Testing and Materials (ASTM) designation (D) 2216 (ASTM, 1990).

Thermal Conductivity

The thermal conductivity of core material was measured in whole-core sections from Holes 1207A, 1208A, and 1209A with the TK04 (Teka Bolin), using the needle-probe method in full-space configuration for soft sediments (von Herzen and Maxwell, 1959). The full-space needle, containing a heater wire and calibrated thermistor, was inserted into the unconsolidated sediment through a small hole drilled into the core liner. Three measuring cycles were automatically performed at each sampling location. At the beginning of each test, a self-test that included a drift study was conducted. Once the samples were equilibrated, the heater circuit was closed and the temperature rise in the probes was recorded. Thermal conductivities were calculated from the rate of temperature rise while the heater current was flowing. Temperatures measured during the first 150 s of the heating cycle were fitted to an approximate solution of a constantly heated line source (for details see Kristiansen, 1982, and Blum, 1997). Measurement errors were 5%–10%. No correction was attempted for in situ temperature or pressure effects. Thermal conductivity was measured only in soft sediments, into which the TK04 needles could be inserted without risk of damage. Measurements of thermal conductivity were not conducted at all Leg 198 sites.

Compressional Wave Velocity

In addition to velocity measurements made with the PWL, compressional wave velocity was measured on split-core sections using the modified Hamilton frame velocimeter (PWS3). The digital sonic velocimeter (DSV) was not used during Leg 198, so the disturbance of sediment cores was minimized. The PWS3 measures the traveltime of a 500-kHz signal directed orthogonally (x-direction) across the split-core section and core liner between two piezoelectric transducers located at opposite sides of the split-sediment core. Sample thickness was measured directly from the velocimeter frame lead screw through a linear resistor output to a digital multimeter. The PWS3 transducers were calibrated using the linear regression of travel time vs. distance for a set of Lucite standards. Split-core velocities were measured perpendicular to the length of the core and were corrected for the presence of the liner. Routine sampling frequency for *P*-wave measurements was one per section, with "exotic" lithologies (e.g., black shale, radiolarite, chert, basalt, and porcellanite) sampled where relevant; the positions of PWS3 *P*-wave measurements were next to those for index properties whenever possible. Deionized water was added to the contact between the transducers and sample to improve acoustic coupling. The velocity data stored in the ODP Janus database are uncorrected for in situ temperature and pressure. However, these corrections can be made using the relation-

ships outlined in Wyllie et al. (1956), Wilson (1960), and Mackenzie (1981).

In Situ Temperature Measurements and Heat Flow Calculations

Downhole temperature measurements were taken at Site 1209 to determine the heat flow on Shatsky Rise. In situ temperature measurements were made using the Adara temperature tool as part of regular APC coring operations. The components of the Adara tool are contained in an annulus in the coring shoe of the APC string and include a platinum temperature sensor and a data logger. The platinum resistance-temperature device is calibrated over a range of 0° to 100°C, with a resolution of 0.01°C. During operation, the coring shoe is attached to a core barrel and lowered down the pipe by wireline. The tool is typically held for 5–10 min at the mudline to equilibrate with bottom-water temperatures then lowered to the end of the drill string. The standard APC coring technique is subsequently used, with the core barrel fired through the drill bit using hydraulic pressure. The Adara tool is left in the sediment for 10–15 min to obtain a temperature record. These data provide a sufficiently long transient record for reliable extrapolation of the steady-state temperature. The nominal accuracy of the Adara temperature measurement is ±0.1°C. These data were combined with measurements of thermal conductivity obtained from whole-core samples to calculate heat flow values.

Depth-Traveltime Conversion

Depths to significant horizons at the Leg 198 sites were converted to traveltime so that horizons could be identified with reflectors in the seismic section. Three different methods of depth-traveltime conversion were employed to provide a gauge of the range of uncertainty in the results because each method carries a different set of assumptions:

1. The empirical depth-traveltime conversion of Carlson et al. (1986) was used as a "standard" depth-traveltime reference. It is based on the depths to 233 horizons at 154 DSDP sites, and the traveltime of the interpreted reflection of those horizons in the seismic lines. The best-fit function to these data is

$$z = -3.02 \ln(1 - 0.53t),$$

   where z = depth (in kilometers) and t = one-way traveltime (in seconds).
2. The PWS velocity measurements made on half-cores were converted to traveltimes. These are likely to be overestimates of the true traveltime, because the sediments are no longer under in situ pressure conditions when they are measured. For Site 1207, downhole log data were used in addition to the core data.
3. Synthetic seismograms were calculated from the PWS velocities and index property density measurements. Patterns of reflections were correlated between the synthetic seismogram and the seismic section, resulting in depth-traveltime tie points. For Site 1207, downhole log data were used in addition to the core data.

It is likely that the synthetic seismograms can be improved post-cruise by incorporating the GRA density core data.

All three methods gave consistent depth-traveltime conversions, to within ~0.01 s two-way traveltime per 100 m of depth. The traveltimes from PWS velocities were the longest at most sites, the traveltimes from the Carlson et al. (1986) empirical formula were the shortest, and the tie points from the synthetic seismograms fell in between. The average of the PWS and empirical traveltimes was used to plot the borehole on the seismic section (see Figs. **F15,** p. 105, **F19,** p. 109, **F25,** p. 115, and **F29,** p. 119, all in the "Leg 198 Summary" chapter). The exceptions to this pattern are Sites 1207 and 1213 (Figs. **F11,** p. 100, and **F35,** p. 125, both in the "Leg 198 Summary" chapter), which penetrate Lower Cretaceous formations containing chert and lithified sediments, where the synthetic seismogram tie points and the traveltimes based on core/log velocities have shorter traveltimes than the Carlson et al. (1986) empirical conversion. For Site 1207, the traveltimes from synthetic seismogram tie points were used to plot the borehole on the seismic section (see Figs. **F61,** p. 114, **F62,** p. 115, both in the "Site 1207" chapter).

DOWNHOLE MEASUREMENTS

Downhole logs are used to determine physical, chemical, and structural properties of the formation penetrated by a borehole. The data are rapidly collected, continuous with depth, and measured in situ; they can be interpreted in terms of the stratigraphy, lithology, mineralogy, and geochemical composition of the penetrated formation. Where core recovery is incomplete or disturbed, log data may provide the only way to characterize the borehole section; where core recovery is good, log and core data complement one another and may be interpreted jointly.

Downhole logs are sensitive to formation properties on a scale that is intermediate between those obtained from laboratory measurements on core samples and geophysical surveys. They are useful in calibrating the interpretation of geophysical survey data (e.g., through the use of synthetic seismograms) and provide a necessary link for the integrated understanding of physical properties on all scales. Wireline logging was performed at Sites 1207 and 1213.

Wireline Logging

During wireline logging, the logs are made with a variety of Schlumberger logging tools combined into several "tool strings," which are run down the hole after coring operations are complete. Three wireline tool strings were used during Leg 198: the triple combination (triple combo) (resistivity, density, and porosity); the Formation MicroScanner (FMS)-sonic (resistivity image of the borehole wall and sonic velocities); and the geological high-resolution magnetic tool (GHMT) (magnetic field strength and magnetic susceptibility) (Fig. **F8;** Table **T7**).

Each tool string also contains a telemetry cartridge for communicating through the wireline to the Schlumberger minimum configuration MAXIS (MCM) unit on the drillship and a natural gamma radiation tool that provides a common reference for correlation and depth shifting between multiple logging runs. Logging runs are typically conducted at 250–300 m/hr.

F8. Schematic illustration of configurations of tool strings, p. 53.

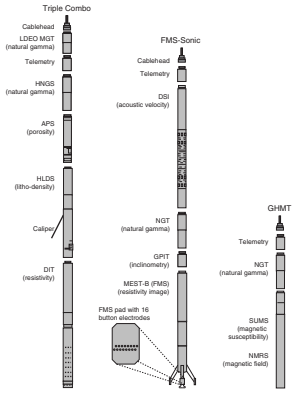

T7. Measurements made by wireline tool strings, p. 62.

In preparation for logging, the boreholes were flushed of debris by circulating a "pill" of viscous drilling fluid (sepiolite mud mixed with seawater; approximate weight = 8.8 lb/gal, or 1.055 g/cm^3) through the drill pipe to the bottom of the hole. The bottom-hole assembly (BHA) was pulled up to a depth of 160 mbsf for the Hole 1207B and 90 mbsf for Hole 1213B, and then run down to the bottom of the hole again to ream borehole irregularities. The holes were subsequently filled with more sepiolite mud, and the pipe was raised to 160 mbsf for Hole 1207B and 126 mbsf for Hole 1213B and kept there to prevent hole collapse during logging. The tool strings were then lowered downhole by a seven-conductor wireline cable during sequential runs. A wireline heave compensator (WHC) was employed to minimize the effect of ship's heave on the tool position in the borehole (Goldberg, 1990). During each logging run, incoming data were recorded and monitored in real time on the MCM logging computer. The tool strings were then pulled up at constant speed to provide continuous measurements as a function of depth of several properties simultaneously.

In addition to the Schlumberger tools, we also used the LDEO multisensor spectral gamma ray tool (MGT) at Hole 1207B; it was positioned at the top of the triple combo tool string. Data from this tool are recorded in real time on the acquisition system in the downhole measurements laboratory (DHML). Data from the MGT and the Schlumberger tools cannot be recorded simultaneously: the MGT requires a second pass in the hole.

Logged Sediment Properties and Tool Measurement Principles

The logged properties, and the methods that the tools use to measure them, are briefly described below. The main logs taken by the tools are listed in Table T8. More detailed information on individual tools and their geological applications may be found in Ellis (1987), Goldberg (1997), Lovell et al. (1998), Rider (1996), Schlumberger (1989, 1994), and Serra (1984, 1986, 1989).

T8. Acronyms and units for wireline tools, p. 63.

Natural Radioactivity

Three wireline spectral gamma ray tools were used to measure and classify natural radioactivity in the formation: the natural gamma ray tool (NGT), the hostile environment natural gamma ray sonde (HNGS) and the LDEO MGT. The NGT uses a sodium iodide scintillation detector and five-window spectroscopy to determine concentrations of K, Th, and U, the three elements whose isotopes dominate the natural radiation spectrum. The HNGS is similar to the NGT, but it uses two bismuth germanate scintillation detectors for a significantly improved tool precision. The HNGS filters out gamma ray energies below 500 keV, eliminating sensitivity to bentonite or KCl in the drilling mud and improving measurement accuracy. Although the NGT response is sensitive to borehole diameter and the density of the drilling mud, corrections for these effects are routinely made during processing at LDEO. See "LDEO Multisensor Spectral Gamma Ray Tool," p. 32, for a description of the MGT.

Density

Formation density was determined with the hostile environment lithodensity sonde (HLDS). The sonde contains a radioactive cesium (^{137}Cs) gamma ray source (622 keV) and far and near gamma ray detectors mounted on a shielded skid, which is pressed against the borehole wall by a hydraulically activated eccentralizing arm. Gamma rays emitted by the source undergo Compton scattering, which involves the transfer of energy from gamma rays to the electrons in the formation via elastic collision. The number of scattered gamma rays that reach the detectors is directly related to the density of electrons in the formation, which is in turn related to bulk density. Porosity may also be derived from this bulk density if the matrix (grain) density is known.

The HLDS also measures photoelectric absorption as the photoelectric effect (PEF). Photoelectric absorption of the gamma rays occurs when they reach <150 keV after being repeatedly scattered by electrons in the formation. Because PEF depends on the atomic number of the elements in the formation, it also varies according to the chemical composition of the minerals present. For example, the PEF of calcite = 5.08 b/e$^-$; illite = 3.03 b/e$^-$; quartz = 1.81 b/e$^-$; and kaolinite = 1.49 b/e$^-$. Good contact between the tool and borehole wall is essential for good HLDS logs; poor contact results in underestimation of density values.

Porosity

Formation porosity was measured with the accelerator porosity sonde (APS). The sonde incorporates a minitron neutron generator that produces fast (14.4 MeV) neutrons and five neutron detectors (four epithermal and one thermal) positioned at different spacings from the minitron. The measurement principle involves counting neutrons that arrive at the detectors after being slowed by atomic nuclei in the formation. The highest energy loss occurs when neutrons collide with hydrogen nuclei, which have practically the same mass as the neutron (the neutrons simply bounce off of heavier elements without losing much energy). If the hydrogen (i.e., water) concentration is low, as in low-porosity formations, neutrons can travel farther before being captured and the count rates increase at the detector. The opposite effect occurs in high porosity formations where the water content is high. However, because hydrogen bound in minerals such as clays or in hydrocarbons also contributes to the measurement, the raw porosity value is often an overestimate.

Upon reaching thermal energies (0.025 eV), the neutrons are captured by the nuclei of Cl, Si, B, and other elements, resulting in a gamma ray emission. This neutron capture cross section (Σ_f) is also measured by the tool.

Electrical Resistivity

The phasor dual induction/spherically focused resistivity tool (DIT) was used to measure electrical resistivity. The DIT provides three measures of electrical resistivity, each with a different depth of investigation into the formation. The two induction devices (deep and medium depths of penetration) transmit high-frequency alternating currents through transmitter coils, creating magnetic fields that induce secondary currents in the formation. These currents produce a new inductive signal, proportional to the conductivity of the formation, which is mea-

sured by the receiving coils. The measured conductivities are then converted to resistivity (in units of ohm-meters). For the shallow penetration resistivity, the current necessary to maintain a constant drop in voltage across a fixed interval is measured; it is a direct measurement of resistivity. Sand grains and hydrocarbons are electrical insulators, whereas ionic solutions and clays are conductors. Electrical resistivity, therefore, can be used to evaluate porosity (via Archie's Law) and fluid salinity.

Acoustic Velocity

The dipole shear sonic imager measures the transit times between sonic transmitters and an array of eight receivers. It combines replicate measurements, thus providing a direct measurement of sound velocity through sediments that is relatively free from the effects of formation damage and an enlarged borehole (Schlumberger, 1989). Along with the monopole transmitters found on most sonic tools, it also has two crossed dipole transmitters, which allow the measurement of shear wave velocity in addition to the compressional wave velocity, even in the slow formations typically encountered during ODP legs.

Formation MicroScanner

The FMS provides high-resolution electrical resistivity–based images of borehole walls. The tool has four orthogonal arms and pads, each containing 16 button electrodes that are pressed against the borehole wall during the recording (Fig. F8). The electrodes are arranged in two diagonally offset rows of eight electrodes each. A focused current is emitted from the button electrodes into the formation, with a return electrode near the top of the tool. The intensity of current passing through the button electrodes is measured. Processing transforms these measurements, which reflect the microresistivity variations of the formation, into continuous spatially oriented high-resolution images that mimic the geologic structures of the borehole wall. Further processing can provide measurements of dip and direction (azimuth) of planar features in the formation.

The development of the FMS tool has added a new dimension to wireline logging (Luthi, 1990; Lovell et al., 1998; Salimullah and Stow, 1992). Features such as bedding, fracturing, slump folding, and bioturbation can be resolved; the fact that the images are oriented means that fabric analysis can be carried out and bed orientations can be measured.

The maximum extension of the caliper arms is 15 in. In holes with a diameter larger than 15 in, the pad contact will be inconsistent, and the FMS images may appear out of focus and too conductive. Irregular (rough) borehole walls will also adversely affect the images if contact with the wall is poor.

Accelerometry and Magnetic Field Measurement

Three-component acceleration and magnetic field measurements were made with the general-purpose inclinometer tool. The primary purpose of this tool, which incorporates a three-component accelerometer and a three-component magnetometer, is to determine the acceleration and orientation of the FMS-sonic tool string during logging. Thus, the FMS images can be corrected for irregular tool motion, and the dip

and direction (azimuth) of features in the FMS image can be determined.

GHMT Tool String

The susceptibility measurement sonde (SUMS) measures magnetic susceptibility by means of low-frequency induction in the surrounding sediment. It responds primarily to magnetic minerals (mainly magnetites, hematite, and iron sulfides), which are typically contained in the detrital sediment fraction.

The nuclear resonance magnetometer sonde (NMRS) measures the total magnetic field using a proton precession magnetometer. The data from the SUMS and the NMRS tools can be used to construct a polarity stratigraphy, using the method outlined below.

The total magnetic field (B) measured in the borehole depends on position (p) and time (t) (Pozzi et al., 1988, 1993):

$$B_0\,(p,t) = B_r\,(p) + B_a\,(p) + B_t\,(p,t) + B_f\,(p),$$

where $B_f\,(p) = B_{fi}\,(p) + B_{fr}\,(p)$.

$B_r\,(p)$ is the Earth's main magnetic field, generated in the Earth's liquid outer core. The field intensity is ~41970 nT for Site 1207. $B_a\,(p)$ is the magnetic field caused by the BHA (up to ~2000 nT, decaying away from the BHA) and crustal heterogeneities. $B_t\,(p,t)$ is the time-varying field (e.g., magnetic storms). Two passes of the GHMT are run to check that this is negligible. $B_{fi}\,(p)$ is the field produced in the borehole by the induced magnetization (J_i) of the sediment that is parallel to $B_0\,(p,t)$ and proportional to the magnetic susceptibility (k):

$$J_i = B_0\,(p,t) \cdot k.$$

$B_{fi}\,(p)$ is then given by

$$B_{fi}\,(p) = (J_i/2) \cdot (1 - 3\sin^2 I),$$

where I is the inclination of the Earth's field at the site.

$B_{fr}\,(p)$ is the field produced in the borehole by the remanent magnetization (J_r) of the sediment, whose polarity we aim to determine. J_r is either parallel (normal polarity) or antiparallel (reversed polarity) to $B\,(p,t)$ if the site has not moved significantly (relative to the magnetic poles) since sediment deposition. We find $B_{fr}\,(p)$ by subtracting $B_r\,(p)$, $B_a\,(p)$, and $B_{fi}\,(p)$ from the total field measurement $B\,(p,t)$.

Under favorable conditions, a magnetostratigraphy is given simply by the sign of $B_{fr}\,(p)$. Further processing, completed on shore, involves regression analysis of $B_{fr}\,(p)$ vs. $B_{fi}\,(p)$ downhole on intervals of various thickness. Correlation indicates normal polarity, and anticorrelation indicates reversed polarity. In the case of the Shatsky Rise sediments, the polarity interpretation is complicated and the sites have moved 30° northward since the Early Cretaceous, so the induced and remanent magnetizations will not be parallel to each other. The GHMT was run at Site 1207; however, both the magnetic field and susceptibility logs were compromised by tool malfunction (see **"Downhole Measurements,"** p. 40, in the "Site 1207" chapter).

LDEO Multisensor Spectral Gamma Ray Tool

The MGT was developed by the LDEO Borehole Research Group to improve the vertical resolution of natural gamma ray logs by using an array of four short detector modules with ~2-ft spacing. Each module comprises a small 2 in × 4 in NaI detector, a programmable 256-channel amplitude analyzer, and an ^{241}Am calibration source. The spectral data are later recalculated to determine the concentration of K, Th, and U radioisotopes. The spectral data from individual modules are sampled four times per second and stacked in real time based on the logging speed. This approach increases vertical resolution by a factor of 2–3 over conventional tools while preserving comparable counting efficiency and spectral resolution. The radius of investigation depends on several factors: hole size, mud density, formation bulk density (denser formations display a slightly lower radioactivity) and the energy of the gamma rays (a higher-energy gamma ray can reach the detector from deeper in the formation).

The MGT also includes an accelerometer to improve data stacking by the precise measurement of tool motion. The MGT is typically deployed on top of the Schlumberger triple combo. It has a specialized telemetry system that requires that the Schlumberger tools be powered off while the MGT is collecting data. Postcruise processing may correct for borehole size and tool sticking, which is assessed by accelerator data recorded in the MGT.

Log Data Quality

The principal influence on log data quality is the condition of the borehole wall. If the borehole diameter is variable over short intervals resulting from washouts during drilling, clay swelling, or ledges caused by layers of harder material, the logs from those tools that require good contact with the borehole wall (i.e., FMS, density, and porosity tools) may be degraded. Deep investigation measurements such as resistivity and sonic velocity, which do not require contact with the borehole wall, are generally less sensitive to borehole conditions. Very narrow ("bridged") sections will also cause irregular log results. The quality of the borehole is improved by minimizing the circulation of drilling fluid while drilling, flushing the borehole to remove debris, and logging as soon as possible after drilling and conditioning are completed.

Log Depth Scales

The depth of the wireline-logged measurement is determined from the length of the logging cable played out at the winch on the ship. The seafloor is identified on the natural gamma log by the abrupt reduction in gamma ray count at the water/sediment boundary (mudline). The coring depth (driller's depth) is determined from the known length of the BHA and pipe stands; the mudline is usually recovered in the first core from the hole.

Discrepancies between the driller's depth and the wireline log depth occur because of core expansion, incomplete core recovery, incomplete heave compensation, and drill pipe stretch in the case of driller's depth. In the case of log depth, these discrepancies occur because of incomplete heave compensation, cable stretch (~1 m/km), and cable slip. Tidal changes in sea level will also have an effect. To minimize the wireline tool motion caused by ship heave, a hydraulic wireline heave com-

pensator adjusts for rig motion during wireline logging operations. The small but significant differences between drill pipe depth and logging depth should be taken into account when using the logs for correlation with core and log measurements. Core measurements such as susceptibility and density can be correlated with the equivalent downhole logs using the Sagan program, which allows shifting of the core depths onto the log depth scale. Precise core-log depth matching is difficult in zones where core recovery is low, because of the inherent ambiguity of placing the recovered section within the cored interval.

Logs from different wireline tool strings will have slight depth mismatches. Distinctive features recorded by the natural gamma tool, run on every tool string, provide correlation and relative depth offsets among the logging runs.

Data Recording and Processing

Data for each logging run were recorded, stored digitally, and monitored in real time using the MCM software. On completion of logging at each hole, data were transferred to the DHML for preliminary interpretation. Basic processing was carried out during the cruise to provide scientists with a comprehensive, quality-controlled downhole logging data set that can be used for comparison, integration, and correlation with other data collected during Leg 198 and other ODP legs. The processing includes depth adjustments to remove depth offsets between data from different logging runs, corrections specific to certain tools and logs, documentation for the logs (with an assessment of log quality), and conversion of the data to a widely accessible format (ASCII for the conventional logs; GIF for the FMS images). Schlumberger GeoQuest's GeoFrame software package is used for most of the processing.

Processed acoustic, caliper, density, gamma ray, magnetic, neutron porosity, resistivity, and temperature data in ASCII format are available (see the **"Related Leg Data"** contents list). A summary of logging highlights is also posted on the LDEO-BRG Web site shortly after the end of each leg.

Core-Log-Seismic Integration

GeoFrame's IESX seismic interpretation software package was used during Leg 198 to display site-survey seismic sections acquired precruise on the *Thompson*. Velocity and density logs were used to create synthetic seismograms, which were overlaid on the seismic section and used to refine the depth-traveltime relation. In this way, lithostratigraphic units in the core are correlated with reflectors and sequences in the seismic section.

REFERENCES

Acton, G.D., Borton, C.J., and the Leg 178 Shipboard Scientific Party, 2001. Palmer Deep composite depth scales for Leg 178 Sites 1098 and 1099. *In* Barker, P.F., Camerlenghi, A., Acton, G.D., and Ramsay, A.T.S. (Eds.), *Proc. ODP, Sci. Results,* 178 [Online]. Available from World Wide Web: <http://www-odp.tamu.edu/publications/178_SR/chap_05/chap_05.htm>. [Cited 2001-08-27]

Alexandrovich, J.M., and Hays, J.D., 1989. High-resolution stratigraphic correlation of ODP 111 Holes 677A and 677B and DSDP Leg 69 Hole 504. *In* Becker, K., Sakai, H., et al., *Proc. ODP, Sci. Results,* 111: College Station, TX (Ocean Drilling Program), 263–276.

ASTM, 1990. Standard method for laboratory determination of water (moisture) content of soil and rock. *Annual Book of ASTM Standards* (Vol. 04.08): Philadelphia (Am. Soc. Testing and Mater.), D 2216–90 (revision of 2216–63, 2216–80).

Backman, J., and Raffi, I., 1997. Calibration of Miocene nannofossil events to orbitally-tuned cyclostratigraphies from Ceara Rise. *In* Shackleton, N.J., Curry, W.B., Richter, C., and Bralower, T.J. (Eds.). *Proc. ODP, Sci. Results,* 154: College Station, TX (Ocean Drilling Program), 83–99.

Balsam, W.L., and Damuth, J.E., 2000. Further investigations of shipboard vs. shore-based spectral data: implications for interpreting Leg 164 sediment composition. *In* Paull, C.K., Matsumoto, R., Wallace, P., and Dillon, W.P. (Eds.), *Proc. ODP, Sci. Results,* 164: College Station, TX (Ocean Drilling Program), 313–324.

Balsam, W.L., Damuth, J.E., and Schneider, R.R., 1997. Comparison of shipboard vs. shore-based spectral data from Amazon-Fan Cores: implications for interpreting sediment composition. *In* Flood, R.D., Piper, D.J.W., Klaus, A., and Peterson, L.C. (Eds.), *Proc. ODP, Sci. Results,* 155: College Station, TX (Ocean Drilling Program), 193–215.

Balsam, W.L., Deaton, B.C., and Damuth, J.E., 1998. The effects of water content on diffuse reflectance measurements of deep-sea core samples: an example from ODP Leg 164 sediments. *Mar. Geol.,* 149:177–189.

Baumgartner, P. O., Bartolini, A., Carter, E. S., Conti, M., Cortese, G., Danelian, T., De Wever, P., Dumitrica, P., Dumitrica-Jud, R., Gorican, S., Guex, J., Hull, D.M., Kito, N., Marcucci, M., Matsuoka, A., Murchey, B., O'Dogherty, L., Savary, J., Vishnevskaya, V., Widz, D., and Yao, A., 1995a. Middle Jurassic to Early Cretaceous radiolarian biochronology of Tethys based on Unitary Associations, Middle Jurassic to Lower Cretaceous radiolaria of Tethys: occurrences, systematics, biochronology. *In* Baumgartner, P.O., O'Dogherty, L., Gorican, S., Urquhart, E., Pillevuit, A., and De Wever, P. (Eds.), *Middle Jurassic to Lower Cretaceous Radiolaria of Tethys: Occurrences, Systematics, Biochronology.* Mem. Geol. (Lausanne), 23:1013–1048.

Baumgartner, P.O., O'Dogherty, L., Gorican, S., Dumitrica-Jud, R., Dumitrica, P., Pillevuit, A., Urquart, E., Matsuoka, A., Danelian, T., Bartolini, A., Carter, E.S., De Wever, P., Kito, N., Marcucci, M., and Steiger, T., 1995b. Radiolarian catalogue and systematics of Middle Jurassic to Early Cretaceous Tethyan genera and species. *In* Baumgartner, P.O., O'Dogherty, L., Gorican, S., Urquhart E., Pillevuit, A., and De Wever, P. (Eds.), *Middle Jurassic to Lower Cretaceous Radiolaria of Tethys: Occurrences, Systematics, Biochronology.* Mem. Geol. (Lausanne), 23:37–685.

Berggren, W.A., Hilgen, F.J., Langereis, C.G., Kent, D.V., Obradovich, J.D., Raffi, I., Raymo, M.E., and Shackleton, N.J., 1995a. Late Neogene chronology: new perspectives in high-resolution stratigraphy. *Geol. Soc. Am. Bull.,* 107:1272–1287.

Berggren, W.A., Kent, D.V., Swisher, C.C., III, and Aubry, M.-P., 1995b. A revised Cenozoic geochronology and chronostratigraphy. *In* Berggren, W.A., Kent, D.V., Aubry, M.-P., and Hardenbol, J. (Eds.), *Geochronology, Time Scales and Global Stratigraphic Correlation.* Spec. Publ.—Soc. Econ. Paleontol. Mineral., 54:129–212.

Berggren, W.A., and Norris, R.D., 1997. Biostratigraphy, phylogeny and systematics of Paleocene trochospiral planktic foraminifera. *Micropaleontol., Suppl.* 1, 43:1–116.

Blum, P., 1997. Physical properties handbook: a guide to the shipboard measurement of physical properties of deep-sea cores. *ODP Tech. Note,* 26 [Online]. Available from World Wide Web: <http://www-odp.tamu.edu/publications/tnotes/tn26/INDEX.HTM>. [Cited 2001-08-27]

Bolli, H.M., Beckmann, J.-P., and Saunders, J.B., 1994. *Benthic Foraminiferal Biostratigraphy of the South Caribbean Region:* Cambridge (Cambridge Univ. Press).

Bolli, H.M., and Saunders, J.B., 1985. Oligocene to Holocene low latitude planktic foraminifera. *In* Bolli, H.M., Saunders, J.B., and Perch-Nielsen, K. (Eds.), *Plankton Stratigraphy:* Cambridge (Cambridge Univ. Press), 155–262.

Bown, P.R. (Ed.), 1999. *Calcareous Nannofossil Biostratigraphy:* London (Chapman and Hall).

Boyce, R.E., 1976. Definitions and laboratory techniques of compressional sound velocity parameters and wet-water content, wet-bulk density, and porosity parameters by gravimetric and gamma-ray attenuation techniques. *In* Schlanger, S.O., Jackson, E.D., et al., *Init. Repts. DSDP,* 33: Washington (U.S. Govt. Printing Office), 931–958.

Bralower, T.J., Fullagar, P.D., Paull, C.K., Dwyer, G.S., and Leckie, R.M., 1997. Mid-Cretaceous strontium-isotope stratigraphy of deep-sea sections. *Geol. Soc. Am. Bull.,* 109:1421–1442.

Bralower, T.J., Leckie, R.M., Sliter, W.V., and Thierstein, H.R., 1995. An integrated Cretaceous microfossil biostratigraphy. *In* Berggren, W.A., Kent, D.V., Aubry, M.-P., and Hardenbol, J. (Eds.), *Geochronology, Time Scales, and Global Stratigraphic Correlation.* Spec. Publ.—Soc. Econ. Paleontol. Mineral., 54:65–79.

Bralower, T.J., Monechi, S., and Thierstein, H.R., 1989. Calcareous nannofossil zonation of the Jurassic-Cretaceous boundary interval and correlation with the geomagnetic polarity timescale. *Mar. Micropaleontol.,* 14:153–235.

Bralower, T.J., Sliter, W.V., Arthur, M.A., Leckie, R.M., Allard, D.J., and Schlanger, S.O., 1993. Dysoxic/anoxic episodes in the Aptian-Albian (Early Cretaceous). *In* Pringle, M.S., Sager, W.W., Sliter, W.V., and Stein, S. (Eds.), *The Mesozoic Pacific: Geology, Tectonics, and Volcanism.* Geophys. Monogr., Am. Geophys. Union, 77:5–37.

Bukry, D., 1973. Low-latitude coccolith biostratigraphic zonation. *In* Edgar, N.T., Saunders, J.B., et al., *Init. Repts. DSDP,* 15: Washington (U.S. Govt. Printing Office), 685–703.

————, 1975. Coccolith and silicoflagellate stratigraphy, northwestern Pacific Ocean, Deep Sea Drilling Project Leg 32. *In* Larson, R.L., Moberly, R., et al., *Init. Repts. DSDP,* 32: Washington (U.S. Govt. Printing Office), 677–701.

Burnett, J.A., 1999. Upper Cretaceous. *In* Bown, P.R. (Ed.), *Calcareous Nannofossil Biostratigraphy:* London (Chapman and Hall), 132–199.

Cande, S.C., and Kent, D.V., 1995. Revised calibration of the geomagnetic polarity timescale for the Late Cretaceous and Cenozoic. *J. Geophys. Res.,* 100:6093–6095.

Carlson, R.L., Gangi, A.F., and Snow, K.R., 1986. Empirical reflection travel time versus depth and velocity versus depth functions for the deep sea sediment column. *J. Geophys. Res.* 91:8249–8266.

Caron, M., 1985. Cretaceous planktic foraminifera. *In* Bolli, H.M., Saunders, J.B., and Perch-Nielsen, K. (Eds.), *Plankton Stratigraphy:* Cambridge (Cambridge Univ. Press), 17–86.

Chaisson, W.P., and Leckie, R.M., 1993. High-resolution Neogene planktonic foraminifer biostratigraphy of Site 806, Ontong Java Plateau (western equatorial Pacific). *In* Berger, W.H., Kroenke, L.W., and Mayer, L.A., et al., *Proc. ODP, Sci. Results,* 130: College Station, TX (Ocean Drilling Program), 137–178.

Chaisson, W.P., and Pearson, P.N., 1997. Planktonic foraminifer biostratigraphy at Site 925: middle Miocene–Pleistocene. *In* Shackleton, N.J., Curry, W.B., Richter, C., and Bralower, T.J. (Eds.), *Proc. ODP, Sci. Results,* 154: College Station, TX (Ocean Drilling Program), 3–31.

Channell, J.E.T., Erba, E., Nakanishi, M., and Tamaki, K.T., 1995. Late Jurassic–Early Cretaceous time scales and oceanic magnetic anomaly block models: *In* Berggren,

W.A., Kent, D.V., Aubry, M.-P., and Hardenbol, J. (Eds.), *Geochronology Time Scales and Global Stratigraphic Correlation*. Spec. Publ.—Soc. Econ. Paleontol. Mineral., 54:51–63.

Curry, W.B., Shackleton, N.J., Richter, C., et al., 1995. *Proc. ODP, Init. Repts.,* 154: College Station, TX (Ocean Drilling Program).

Davis, E.E., Mottl, M.J., Fisher, A.T., et al., 1992. *Proc. ODP, Init. Repts.,* 139: College Station, TX (Ocean Drilling Program).

Droser, M.L., and Bottjer, D.J., 1986. A semiquantitative field classification of ichnofabric. *J. Sediment. Petrol.,* 56:558–559.

Ellis, D.V., 1987. *Well Logging for Earth Scientists:* New York (Elsevier).

Emeis K.C., and Kvenvolden, K.A., 1986. Shipboard organic geochemistry on the *JOIDES Resolution*. *ODP Tech. Note,* 7.

Erba, E., Channell, E.T., Claps, M., Jones, C., Larson, R., Opdyke, B., Premoli Silva, I., Riva, A., Salvini, G., and Torricelli, S., 1999. Integrated stratigraphy of the Cismon APTICORE (southern Alps, Italy): a "reference section" for the Barremian-Aptian interval at low latitudes. *J. Foraminiferal Res.,* 29:371–391.

Erba, E., Premoli Silva, I., Wilson, P.A., Pringle, M.S., Sliter, W.V., Watkins, D.K., Arnaud Vanneau, A., Bralower, T.J., Budd, A.F., Camoin, G.F., Masse, J.-P., Mutterlose, J., and Sager, W.W., 1995. Synthesis of stratigraphies from shallow-water sequences at Sites 871 through 879 in the western Pacific Ocean. *In* Haggerty, J.A., Premoli Silva, I., Rack, F., and McNutt, M.K. (Eds.), *Proc. ODP, Sci. Results,* 144: College Station, TX (Ocean Drilling Program), 873–885.

Espitalié, J., Deroo, G., and Marquis, F., 1986. La pyrolyse Rock-Eval et ses applications, Partie III. *Rev. Inst. Fr. Pet.,* 41:73–89.

Exon, N.F., Kennett, J.P., Malone, M.J., et al., 2001. *Proc. ODP, Init. Repts.,* 189 [CD-ROM]. Available from: Ocean Drilling Program, Texas A&M University, College Station TX 77845-9547, USA.

Farrell, J.W., and Janecek, T.R., 1991. Late Neogene paleoceanography and paleoclimatology of the northeast Indian Ocean (Site 758). *In* Weissel, J., Peirce, J., Taylor, E., Alt, J., et al., *Proc. ODP, Sci. Results,* 121: College Station, TX (Ocean Drilling Program), 297–355.

Gieskes, J., Gamo, T., and Brumsack, H.-J., 1991. Chemical methods for interstitial water analysis aboard *JOIDES Resolution*. *ODP Tech. Note,* 15.

Goldberg, D., 1990. Test performance of the Ocean Drilling Program wireline heave motion compensator. *Sci. Drill.,* 1:206–209.

————, 1997. The role of downhole measurements in marine geology and geophysics. *Rev. Geophys.,* 35:315–342.

Gradstein, F.M., 1978. Biostratigraphy of Lower Cretaceous Blake Nose and Blake Bahama Basin foraminifera, DSDP Leg 44, western North Atlantic Ocean. *In* Benson, W.E., Sheridan, R.E., et al., *Init. Repts. DSDP,* 44: Washington (U.S. Govt. Printing Office), 663–702.

Gradstein, F.M., Agterberg, F.P., Ogg, J.G., Hardenbol, J., van Veen, P., Thierry, J., and Huang, Z., 1995. A Triassic, Jurassic and Cretaceous time scale. *In* Berggren, W.A., Kent, D.V., Aubry, M.P., and Hardenbol, J. (Eds.), *Geochronology, Time Scales and Global Stratigraphic Correlation*. Spec. Publ.—Soc. Econ. Paleontol. Mineral., 54:95–126.

Hagelberg, T., Shackleton, N., Pisias, N., and Shipboard Scientific Party, 1992. Development of composite depth sections for Sites 844 through 854. *In* Mayer, L., Pisias, N., Janecek, T., et al., *Proc. ODP, Init. Repts.,* 138 (Pt. 1): College Station, TX (Ocean Drilling Program), 79–85.

Hagelberg, T.K., Pisias, N.G., Shackleton, N.J., Mix, A.C., and Harris, S., 1995. Refinement of a high-resolution, continuous sedimentary section for studying equatorial Pacific Ocean paleoceanography, Leg 138. *In* Pisias, N.G., Mayer, L.A., Janecek, T.R., Palmer-Julson, A., and van Andel, T.H. (Eds.), *Proc. ODP, Sci Results,* 138: College Station, TX (Ocean Drilling Program), 31–46.

Holbourn, A., Kuhnt, W., and Soeding, E., 2001. Atlantic paleobathymetry, paleoproductivity and paleocirculation in the late Albian: the benthic foraminiferal record. *Palaeogeogr., Palaeoclimatol., Palaeoecol.,* 170:171–196.

Holbourn, A.E.L., and Kaminski, M.A., 1997. *Lower Cretaceous Deep-Water Benthic Foraminifera of the Indian Ocean*. Spec. Publ.—Grzybowski Found., 4.

Hoppie, B.W., Blum, P., and the Shipboard Scientific Party, 1994. Natural gamma-ray measurements on ODP cores: introduction to procedures with examples from Leg 150. *In* Mountain, G.S., Miller, K.G., Blum, P., et al., *Proc. ODP, Init. Repts.,* 150: College Station, TX (Ocean Drilling Program), 51–59.

Jansen, E., Raymo, M.E., Blum, P., et al., 1996. *Proc. ODP, Init. Repts.,* 162: College Station, TX (Ocean Drilling Program).

Kaiho, K., 1992. Eocene to Quaternary benthic foraminifers and paleobathymetry of the Izu-Bonin Arc, Legs 125 and 126. *In* Taylor, B., Fujioka, K., et al., *Proc. ODP, Sci. Results,* 126: College Station, TX (Ocean Drilling Program), 285–310.

————, 1998. Phylogeny of deep-sea calcareous trochospiral benthic foraminifera: evolution and diversification. *Micropaleontology,* 44:291–311.

————, 1999. Evolution in the test size of deep-sea benthic foraminifera during the past 120 million years. *Mar. Micropaleontol.,* 37:53–65.

Kameo, K., and Bralower, T.J., 2000. Neogene calcareous nannofossil biostratigraphy of Sites 998, 999, and 1000, Caribbean Sea. In Leckie, R.M., Sigurdsson, H., Acton, G.D., and Draper, G. (Eds.), Proc. ODP, Sci. Results, 165: College Station, TX (Ocean Drilling Program), 3–17.

Keene, J.B., 1975. Cherts and porcellanites from the North Pacific DSDP, Leg 32. *In* Larson, R.L., Moberly, R., et al. *Init. Repts. DSDP,* 32: Washington (U.S. Govt. Printing Office), 429–507.

Kennett, J.P., and Srinivasan, M.S., 1983. *Neogene Planktonic Foraminifera: A Phylogenetic Atlas:* Stroudsberg, PA (Hutchinson Ross).

Kristiansen, J.I., 1982. The transient cylindrical probe method for determination of thermal parameters of earth materials [Ph.D. dissert.]. Aarhus Univ.

Kvenvolden, K.A., and McDonald, T.J., 1986. Organic geochemistry on the *JOIDES Resolution*—an assay. *ODP Tech. Note,* 6.

Leckie, R.M., 1984. Mid-Cretaceous planktonic foraminiferal biostratigraphy off central Morocco, DSDP Leg 79, Sites 545 and 547. *In* Winterer, E.L., Hinz, K., et al., *Init. Repts. DSDP,* 79: Washington (U.S. Govt. Printing Office), 579–620.

Leckie, R.M., Farnham, C., and Schmidt, M.G., 1993. Oligocene planktonic foraminifer biostratigraphy of Hole 803D (Ontong Java Plateau) and Hole 628A (Little Bahama Bank), and comparison with the southern high latitudes. *In* Berger, W.H., Kroenke, L.V., and Mayer, L.A., *Proc. ODP, Sci. Results,* 130: College Station, TX (Ocean Drilling Program), 113–136.

Loeblich, A.R., Jr., and Tappan, H., 1988. Foraminiferal evolution, diversification, and extinction. *J. Paleontol.,* 62:695–714.

Longoria, J.F., 1974. Stratigraphic, morphologic and taxonomic studies of Aptian planktonic foraminifera. *Rev. Esp. Micropaleontol.,* Num. Extraordinario.

Lovell, M.A., Harvey, P.K., Brewer, T.S., Williams, C., Jackson, P.D., and Williamson, G., 1998. Application of FMS images in the Ocean Drilling Program: an overview. *In* Cramp, A., MacLeod, C.J., Lee, S.V., and Jones, E.J.W. (Eds.), *Geological Evolution of Ocean Basins: Results from the Ocean Drilling Program*. Spec. Publ.—Geol. Soc. London, 131:287–303.

Luterbacher, H., 1973. Early Cretaceous foraminifera from the northwestern Pacific: Leg 32 of the Deep Sea Drilling Project. *In* Larson, R.L., Moberly, R., et al., *Init. Reports DSDP,* 32: Washington (U.S. Govt. Printing Office), 703–718.

Luthi, S.M., 1990. Sedimentary structures of clastic rocks identified from electrical borehole images. *In* Hurst, A., Lovell, M.A., and Morton, A.C. (Eds.), *Geological Applications of Wireline Logs*. Spec. Publ.—Geol. Soc. London, 48:3–10.

Lyle, M., Koizumi, I., Richter, C., et al., 1997. *Proc. ODP, Init. Repts.,* 167: College Station, TX (Ocean Drilling Program).

Mackenzie, K.V., 1981. Nine-term equation for sound speed in the oceans. *J. Acoust. Soc. Am.,* 70:807–812.

MacKenzie, W.S., Donaldson, C.H., and Guilford, C., 1982. *Atlas of Igneous Rocks and their Textures:* Harlow, England (Longman).

Manheim, F.T., and Sayles, F.L., 1974. Composition and origin of interstitial water of marine sediments based on deep sea drill cores. *In* Goldberg, E.D. (Ed.), *The Sea* (Vol. 5): *Marine Chemistry: The Sedimentary Cycle:* New York (Wiley), 527–568.

Mazzullo, J., Meyer, A., and Kidd, R., 1988. New sediment classification scheme for the Ocean Drilling Program. *In* Mazzullo, J., and Graham, A.G. (Eds.), *Handbook for Shipboard Sedimentologists. ODP Tech. Note,* 8.

Meyers, P.A., 1994. Preservation of elemental and isotopic source identification of sedimentary organic matter. *Chem. Geol.,* 144:289–302.

Müller, P.J., 1977. C/N ratios in Pacific deep-sea sediments; effect of inorganic ammonium and organic nitrogen compounds sorbed by clays. *Geochim. Cosmochim. Acta,* 41:765–776.

Murray, R.W., Miller, D.J., and Kryc, K.A., 2000. Analysis of major and trace elements in rocks, sediments, and interstitial waters by inductively coupled plasma emission spectrometry (ICP-AES). *ODP Tech. Note,* 29. Available from World Wide Web: <http://www-odp.tamu.edu/publications/tnotes/tn29/INDEX.HTM>. [Cited 2001-08-27]

Nederbragt, A.J., 1990. Biostratigraphy and paleoceanographic potential of the Cretaceous planktic foraminifera Heterohelicidae. [Ph.D. thesis]. Centrale Huisdrukkerij Vrije Univ., Amsterdam.

————, 1991. Late Cretaceous biostratigraphy and development of Heterohelicidae planktic foraminifera. *Micropaleontology,* 37:329–372.

Norris, R.D., 1998. Planktonic foraminifer biostratigraphy: eastern equatorial Atlantic. *In* Mascle, J., Lohmann, G.P., and Moullade, M. (Eds.), *Proc. ODP, Sci. Results,* 159: College Station, TX (Ocean Drilling Program), 445–479.

Nyong, E.E., and Olsson, R.K., 1984. A paleoslope model of Campanian to lower Maastrichtian foraminifera in the North American Basin and adjacent continental margin. *Mar. Micropaleontol.,* 8:437–477.

Okada, H., and Bukry, D., 1980. Supplementary modification and introduction of code numbers to the low-latitude coccolith biostratigraphic zonation (Bukry, 1973; 1975). *Mar. Micropaleontol.,* 5:321–325.

Olsson, R.K., Hemleben, C., Berggren, W.A., and Huber, B.T. (Eds.), 1999. *Atlas of Paleocene Planktonic Foraminifera.* Smithsonian Contrib. Paleobiol., 85.

Pearson, P.N., 1995. Planktonic foraminifer biostratigraphy and the development of pelagic caps on guyots in the Marshall Islands Group. *In* Haggerty, J., Premoli Silva, I., Rack, F., and McNutt, M.K. (Eds.), *Proc. ODP, Sci. Results,* 144: College Station, TX (Ocean Drilling Program), 21–59.

Pearson, P.N., and Chaisson, W.P., 1997. Late Paleocene to middle Miocene planktonic foraminifer biostratigraphy of the Ceara Rise. *In* Shackleton, N.J., Curry, W.B., Richter, C., and Bralower, T.J. (Eds.), *Proc. ODP, Sci. Results,* 154: College Station, TX (Ocean Drilling Program), 33–68.

Perch-Nielsen, K., 1985. Mesozoic calcareous nannofossils. *In* Bolli, H.M., Saunders, J.B., and Perch-Nielsen, K. (Eds.), *Plankton Stratigraphy:* Cambridge (Cambridge Univ. Press), 329–426.

Petrizzo, M.R., 2000. Upper Turonian–lower Campanian planktonic foraminifera from southern mid-high latitudes (Exmouth Plateau, NW Australia): biostratigraphy and taxonomic notes. *Cretaceous Res.,* 21:479–505.

Pflum, C.E., and Frerichs, W.E., 1976. Gulf of Mexico deep-water foraminifers. *Spec. Publ.—Cushman Found. Foraminiferal Res.,* 14:1-122.

Pimmel, A., and Claypool, G., 2001. Introduction to shipboard organic geochemistry on the *JOIDES Resolution. ODP Tech. Note,* 30 [Online]. Available from World Wide Web: <http://www-odp.tamu.edu/publications/tnotes/tn30/INDEX.HTM>. [Cited 2001-08-27]

Postuma, J.A., 1971. *Manual of Planktonic Foraminifera:* Amsterdam (Elsevier).

Pozzi, J.-P., Barthes, V., Thibal, J., Pocachard, J., Lim., M., Thomas, T., and Pages, G. 1993. Downhole magnetostratigraphy in sediments: Comparison with the paleomagnetism of a core. *J. Geophys. Res.* 98: 7939–7957.

Pozzi, J.-P., Martin, J.-P., Pocachard, J., Feinberg, H., and Galdeano, A. 1988. In-situ magnetostratigraphy: interpretation of magnetic logging in sediments. *Earth Planet. Sci. Lett.,* 88:357–373.

Premoli Silva, I., and Sliter, W.V., 1994. Cretaceous planktonic foraminiferal biostratigraphy and evolutionary trends from the Bottaccione Section, Gubbio, Italy. *Palaeontogr. Ital.,* 82:2–90.

————, 1999. Cretaceous paleoceanography: evidence from planktonic foraminiferal evolution. *In* Barrera, E., and Johnson, C.C. (Eds.), *The Evolution of the Cretaceous Ocean-Climate System.* Spec. Pap.—Geol. Soc. Am., 332:301–328.

Raffi, I., and Flores, J.-A., 1995. Pleistocene through Miocene calcareous nannofossils from eastern equatorial Pacific Ocean. *In* Pisias, N.G., Mayer, L.A., Janecek, T.R., Palmer-Julson, A., and van Andel, T.H. (Eds.), *Proc. ODP, Sci. Results,* 138: College Station, TX (Ocean Drilling Program), 233–286.

Rider, M., 1996. *The Geological Interpretation of Well Logs* (2nd ed.): Caithness (Whittles Publishing).

Robaszynski, F., Caron, M. (Coord.), and the European Working Group on Planktonic Foraminifera, 1979. *Atlas de Foraminifères Planctoniques du Crétacé Moyen* (Vols. 1 and 2). Cah. Micropaleontol.

Robaszynski, F., Caron, M., Gonzalez-Donoso, J.-M., Wonders, A.A.H., and the European Working Group on Planktonic Foraminifera, 1984. Atlas of Late Cretaceous Globotruncanids. *Rev. Micropaleontol.,* 26:145–305.

Rock-Color Chart Committee, 1991. *Rock Color Charts*. Geological Society of America.

Roth, P.H., 1973. Calcareous nannofossils—Leg 17, Deep Sea Drilling Project. *In* Winterer, E.L., Ewing, J.I., et al., *Init. Repts. DSDP,* 17: Washington (U.S. Govt. Printing Office), 695–795.

————, 1978. Cretaceous nannoplankton biostratigraphy and oceanography of the northwestern Atlantic Ocean. *In* Benson, W.E., Sheridan, R.E., et al., *Init. Repts. DSDP,* 44: Washington (U.S. Govt. Printing Office), 731–759.

————, 1983. Jurassic and Lower Cretaceous calcareous nannofossils in the western North Atlantic (Site 534): biostratigraphy, preservation, and some observations on biogeography and paleoceanography. *In* Sheridan, R.E., Gradstein, F.M., et al., *Init. Repts. DSDP,* 76: Washington (U.S. Govt. Printing Office), 587–621.

Ruddiman, W.F., Cameron, D., and Clement, B.M., 1987. Sediment disturbance and correlation of offset holes drilled with the hydraulic piston corer: Leg 94. *In* Ruddiman, W.F., Kidd, R.B., Thomas, E., et al., *Init. Repts. DSDP,* 94 (Pt. 2): Washington (U.S. Govt. Printing Office), 615–634.

Sacks, I.S., Suyehiro, K., Acton, G.D., et al., 2000. *Proc. ODP, Init. Repts.,* 186 [CD-ROM]. Available from: Ocean Drilling Program, Texas A&M University, College Station, TX 77845-9547, USA.

Salimullah, A.R.M., and Stow, D.A.V., 1992. Application of FMS images in poorly recovered coring intervals: examples from ODP Leg 129. *In* Hurst, A., Griffiths, C.M., and Worthington, P.F. (Eds.), *Geological Application of Wireline Logs II*. Spec. Publ.—Geol. Soc. London, 65:71–86.

Schlumberger, 1989. *Log Interpretation Principles/Applications:* Houston (Schlumberger Educ. Services), SMP–7017.

————, 1994. *IPL Integrated Porosity Lithology:* Houston (Schlumberger Wireline and Testing), SMP-9270.

Serra, O., 1984. *Fundamentals of Well-Log Interpretation* (Vol. 1): *The Acquisition of Logging Data:* Dev. Pet. Sci., 15A.

————, 1986. *Fundamentals of Well-Log Interpretation* (Vol. 2): The *Interpretation of Logging Data*. Dev. Pet. Sci., 15B.

————————, 1989. *Formation MicroScanner Image Interpretation:* Houston (Schlumberger Educ. Services), SMP-7028.

Shackleton, N.J., Baldauf, J.G., Flores, J.-A., Iwai, M., Moore, T.C., Jr., Raffi, I., and Vincent, E., 1995. Biostratigraphic summary for Leg 138. *In* Pisias, N.G., Mayer, L.A., Janecek, T.R., Palmer-Julson, A., and van Andel, T.H. (Eds.), *Proc. ODP, Sci. Results,* 138: College Station, TX (Ocean Drilling Program), 517–536.

Shipboard Scientific Party, 1992. Explanatory notes. *In* Mayer, L., Pisias, N., Janeck, T., et al., *Proc. ODP, Init. Repts.,* 138 (Pt. 1): College Station, TX (Ocean Drilling Program), 13–42.

————————, 1999. Explanatory notes. *In* Gersonde, R., Hodell, D.A., Blum, P., et al., *Proc. ODP, Init. Repts.,* 177, 1–57 [CD-ROM]. Available from: Ocean Drilling Program, Texas A&M University, College Station, TX 77845-9547, U.S.A.

————————, 2001. Explanatory notes. *In* Exon, N.F., Kennett, J.P., Malone, M.J., et al., *Proc. ODP, Init. Repts.,* 189, 1–59 [CD-ROM]. Available from: Ocean Drilling Program, Texas A&M University, College Station TX 77845-9547, USA.

Sissingh, W., 1977. Biostratigraphy of Cretaceous calcareous nannoplankton. *Geol. Mijnbouw,* 57:433–440.

Sliter, W.V., 1977. Cretaceous benthic foraminifers from the western South Atlantic Leg 39, Deep Sea Drilling Project. *In* Supko, P.R., Perch-Nielsen, K., et al., *Init. Repts. DSDP,* 39: Washington (U.S. Govt. Printing Office), 657–697.

————————, 1980. Mesozoic foraminifers and deep-sea benthic environments from Deep Sea Drilling Project Sites 415 and 416, eastern North Atlantic. *In* Lancelot, Y., Winterer, E.L., et al., *Init. Repts. DSDP,* 50: Washington (U.S. Govt. Printing Office), 353–427.

————————, 1989. Biostratigraphic zonation for Cretaceous planktonic foraminifers examined in thin section. *J. Foraminiferal Res.,* 19:1–19.

Spezzaferri, S., 1994. Planktonic foraminiferal biostratigraphy and taxonomy of the Oligocene and lower Miocene in the oceanic record: an overview. *Palaeontographica Ital.,* 81:1–187.

Spezzaferri, S., and Premoli Silva, I., 1991. Oligocene planktonic foraminiferal biostratigraphy and paleoclimatic interpretation from Hole 538A, DSDP Leg 77, Gulf of Mexico. *Palaeogeogr., Palaeoclimatol., Palaeoecol.,* 83: 217–263.

Stein, R., Brass, G., Graham, D., Pimmel, A., and the Shipboard Scientific Party, 1995. Hydrocarbon measurements at Arctic Gateways sites (ODP Leg 151). *In* Myhre, A.M., Thiede, J., Firth, J.V., et al., *Proc. ODP, Init. Repts.,* 151: College Station, TX (Ocean Drilling Program), 385–395.

Tjalsma, R.C., and Lohmann, G.P., 1983. Paleocene–Eocene bathyal and abyssal benthic foraminifera from the Atlantic Ocean. *Micropaleontol. Spec. Publ.,* 4.

Toumarkine, M., and Luterbacher, H., 1985. Paleocene and Eocene planktic foraminifera. *In* Bolli, H.M., Saunders, J.B., and Perch-Nielsen, K. (Eds.), *Plankton Stratigraphy:* Cambridge (Cambridge Univ. Press), 87–154.

van Morkhoven, F.P.C.M., Berggren, W.A., and Edwards, A.S., 1986. Cenozoic cosmopolitan deep-water benthic foraminifera. *Bull. Cent. Rech. Explor.—Prod. Elf-Aquitaine,* 11.

von Herzen, R. P., and Maxwell, A.E., 1959, The measurement of thermal conductivity of deep-sea sediments by a needle-probe method. *J. Geophys. Res.,* 64:1557–1563.

Wentworth, C.K., 1922. A scale of grade and class terms of clastic sediments. *J. Geology,* 30: 377–392.

Wilson, W. D., 1960. Speed of sound in seawater as a function of temperature, pressure and salinity. *J. Acoust. Soc. Am.,* 32:641–644.

Woodruff, F., 1985. Changes in Miocene deep-sea benthic foraminferal distribution in the Pacific Ocean: relationship to paleoceanography. In Kennett, J.P. (Ed.), The Miocene Ocean: Paleoceanography and Biogeography. Mem.—Geol. Soc. Am., 163:131–175.

Wyllie, M.R.J., Gregory, A.R., and Gardner, L.W., 1956. Elastic wave velocities in heterogeneous and porous media. *Geophysics,* 21:41–70.

Figure F1. Key to symbols used in the graphic lithology column log on the computer-generated core description forms.

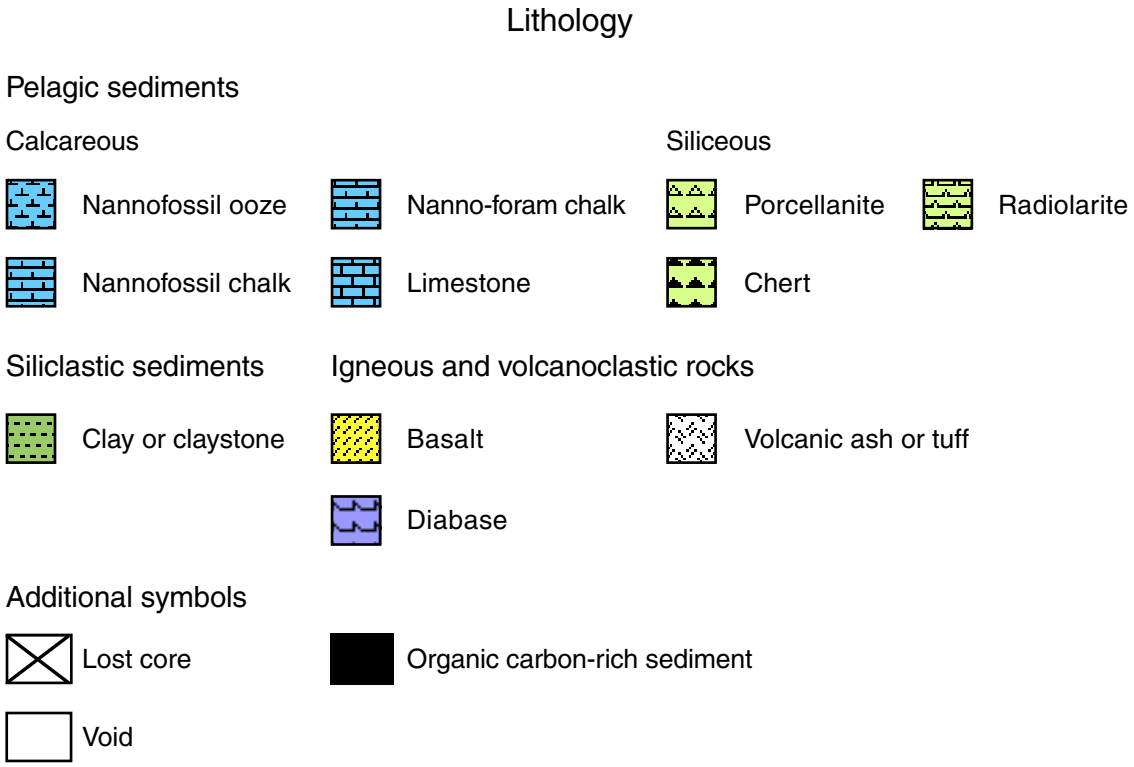

Figure F2. Key to symbols used for contacts, physical structures, lithologic accessories, ichnofossils, fossils, core disturbance, and bioturbation on the computer-generated core description forms.

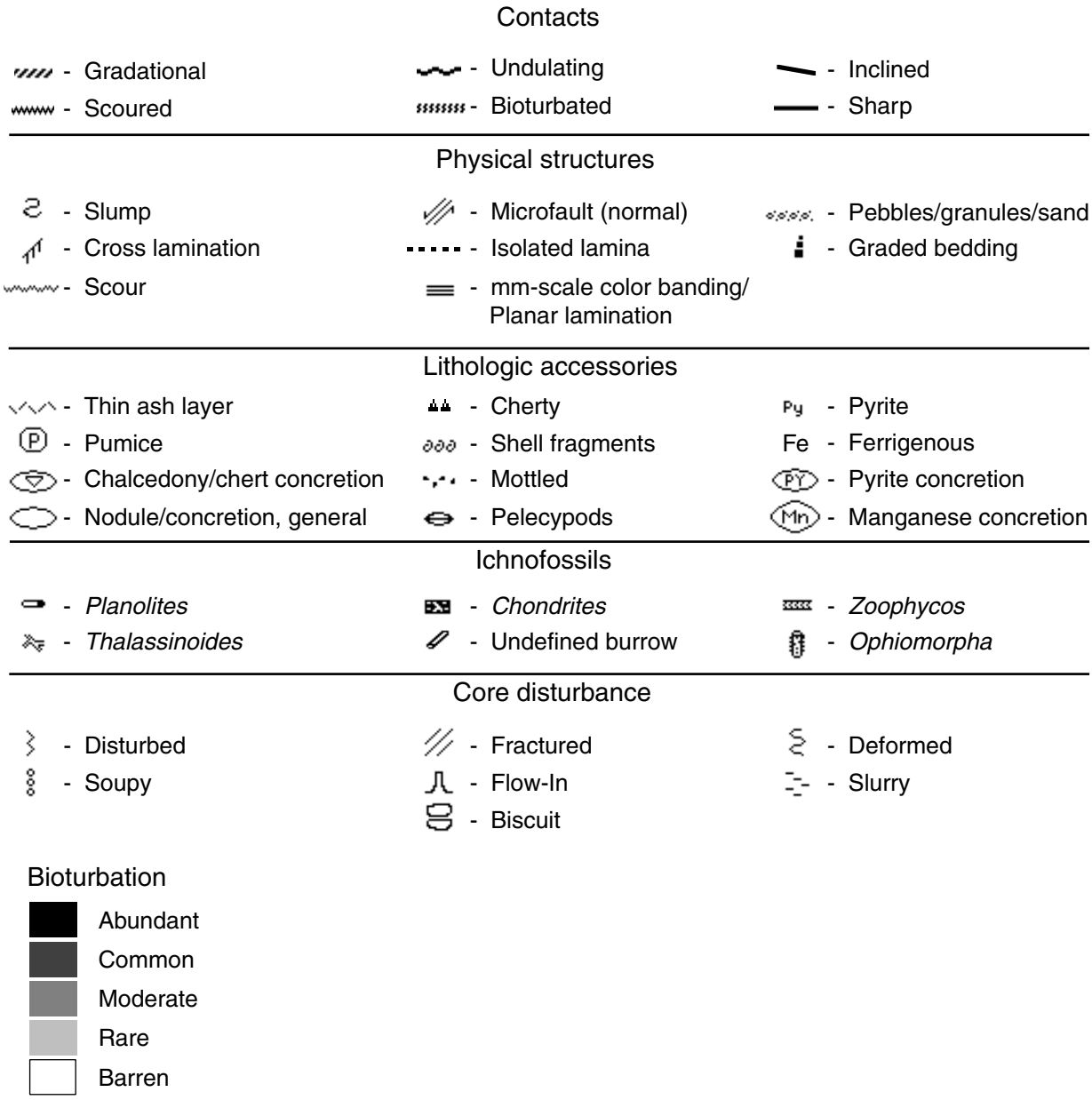

Figure F3. Grain-size divisions for sedimentary rocks (adapted from Wentworth, 1922).

Millimeters (mm)	Micrometers (μm)	Phi (f)	Wentworth size class		Rock type
4096		-12.0	Boulder		Conglomerate/ Breccia
256		-8.0	Cobble	Gravel	
64		-6.0	Pebble		
4		-2.0	Granule		
2.00		-1.0	Very coarse sand		Sandstone
1.00		0.0	Coarse sand		
1/2 0.50	500	1.0	Medium sand	Sand	
1/4 0.25	250	2.0	Fine sand		
1/8 0.125	125	3.0	Very fine sand		
1/16 0.0625	63	4.0	Coarse silt		Siltstone
1/32 0.031	31	5.0	Medium silt		
1/64 0.0156	15.6	6.0	Fine silt	Silt	
1/128 0.0078	7.8	7.0	Very fine silt		
1/256 0.0039	3.9	8.0			
0.00006	0.06	14.0	Clay	Mud	Claystone

Figure F4. Leg 198 timescale and primary calcareous microfossil datums for the Cenozoic and Cretaceous. T = datum top or last occurrence, B = datum base or first occurrence, TA = top of acme. Burdigal. = Burdigalian. (Continued on next four pages.)

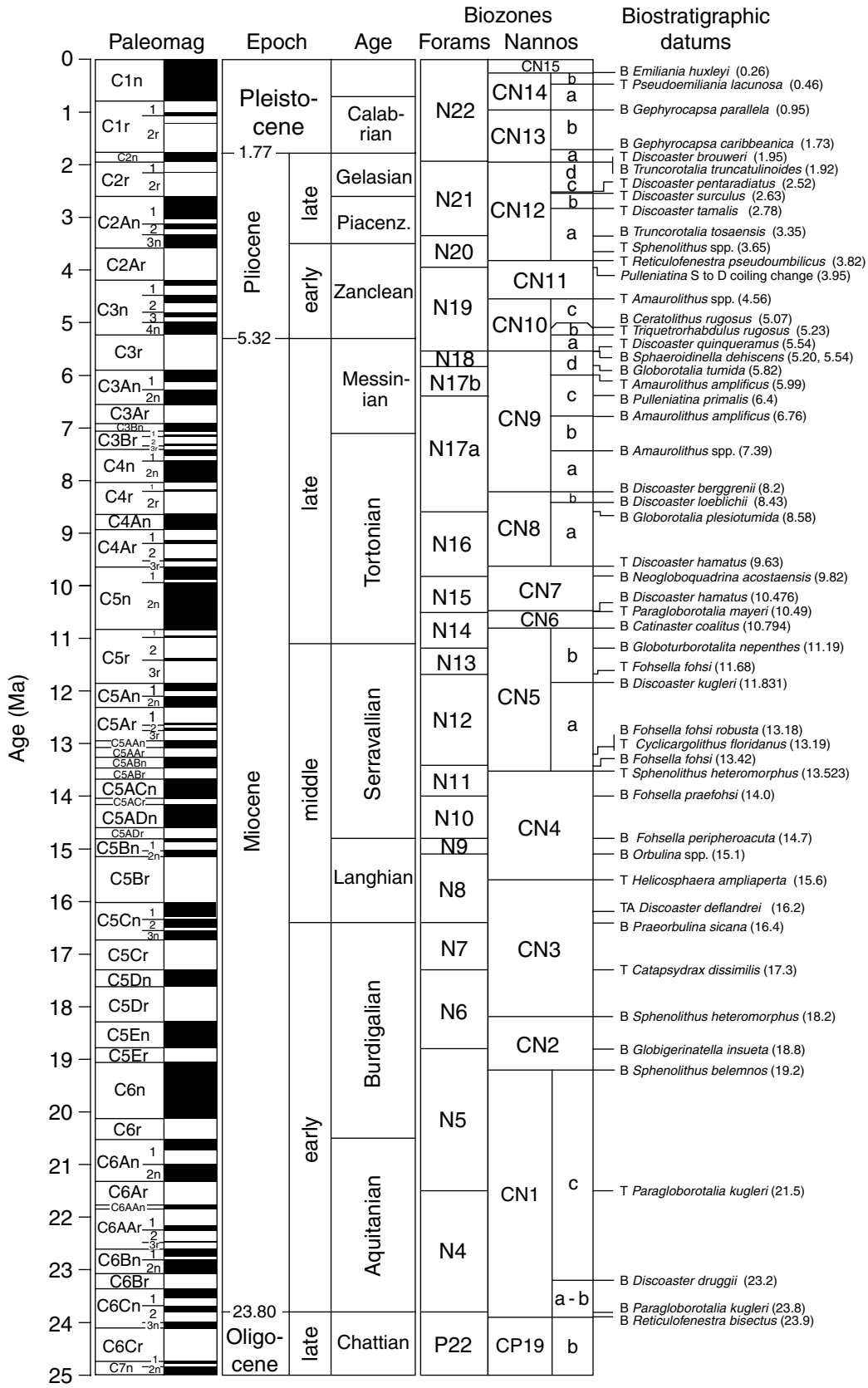

Figure F4 (continued).

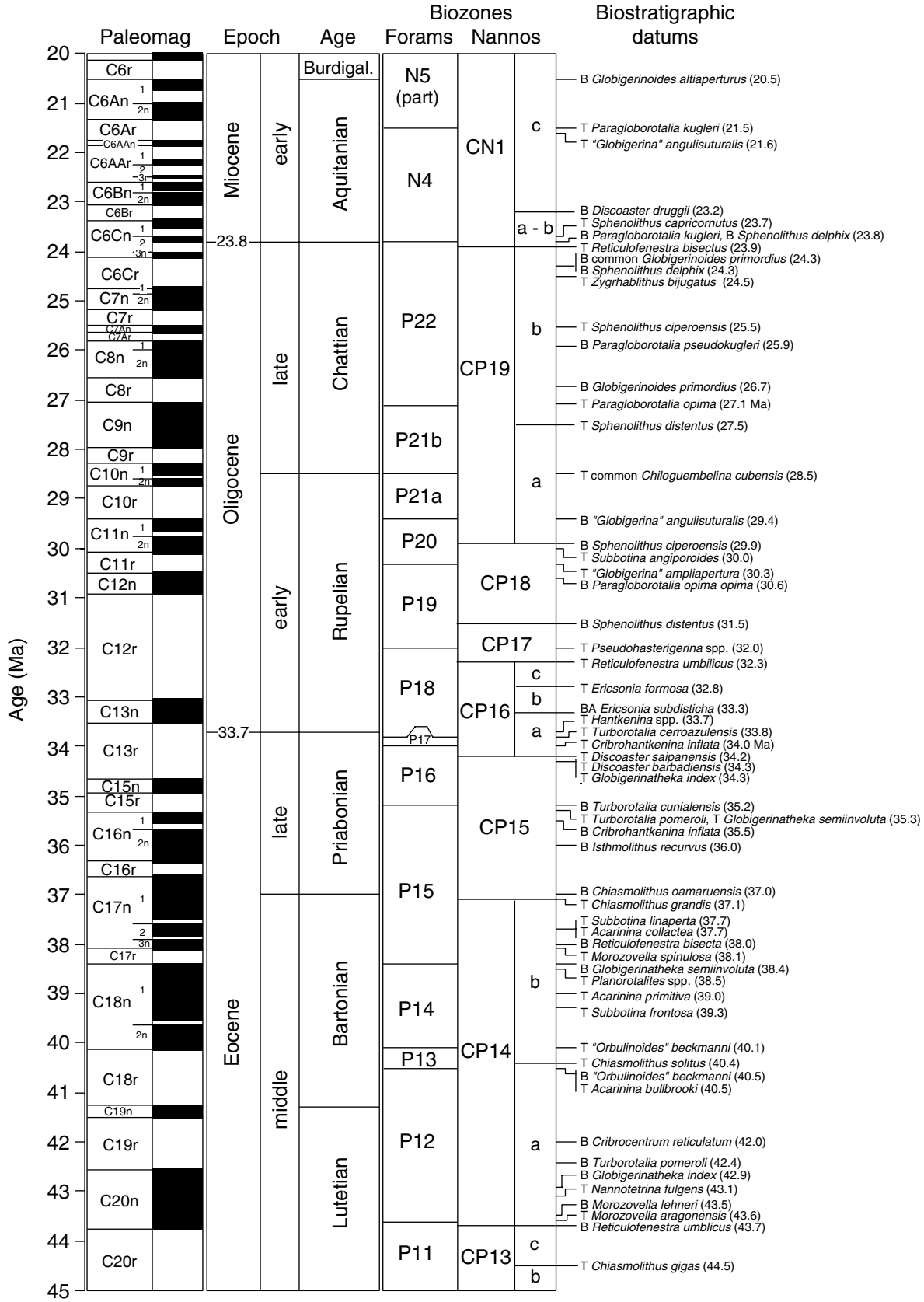

Figure F4 (continued).

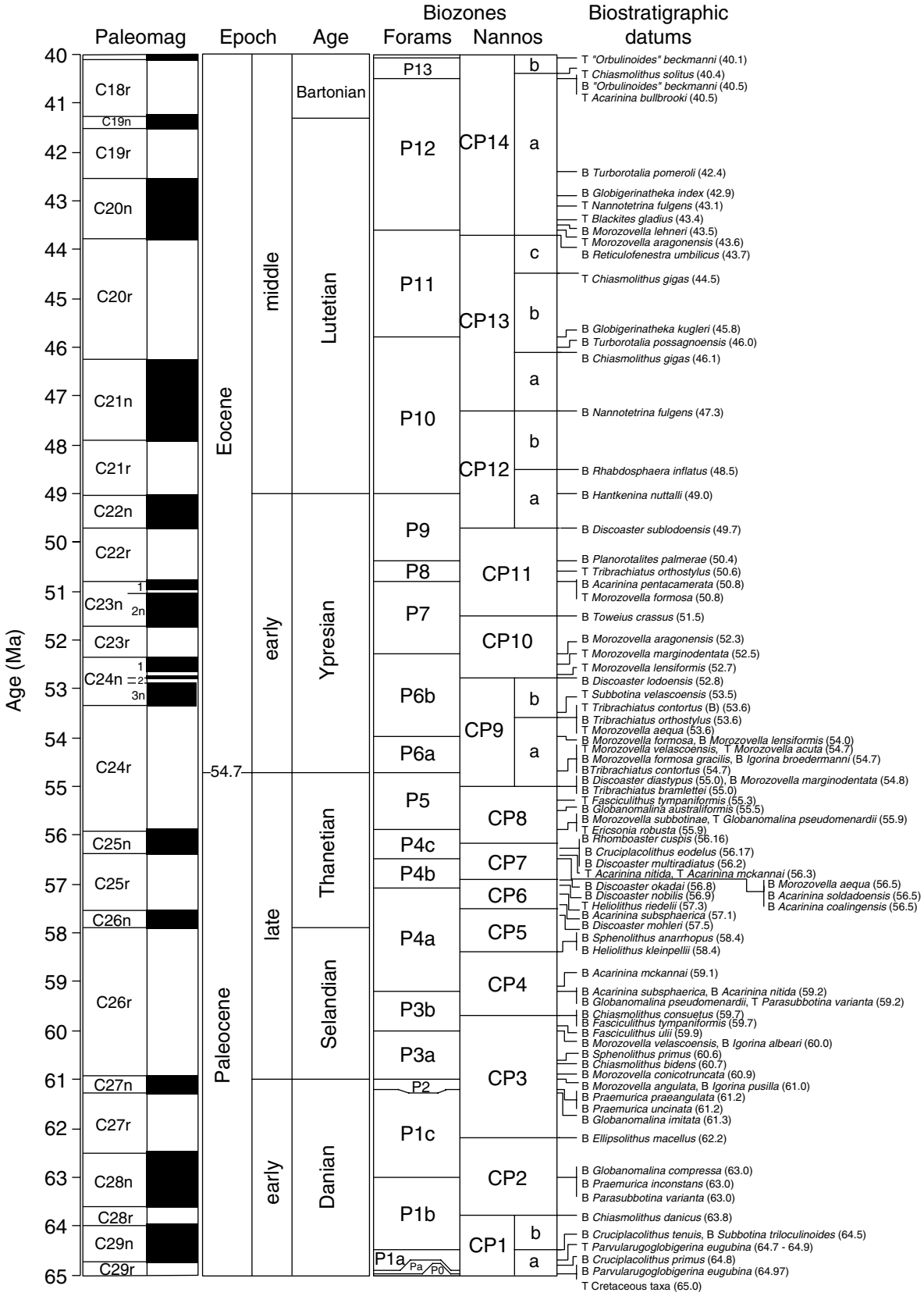

Figure F4 (continued).

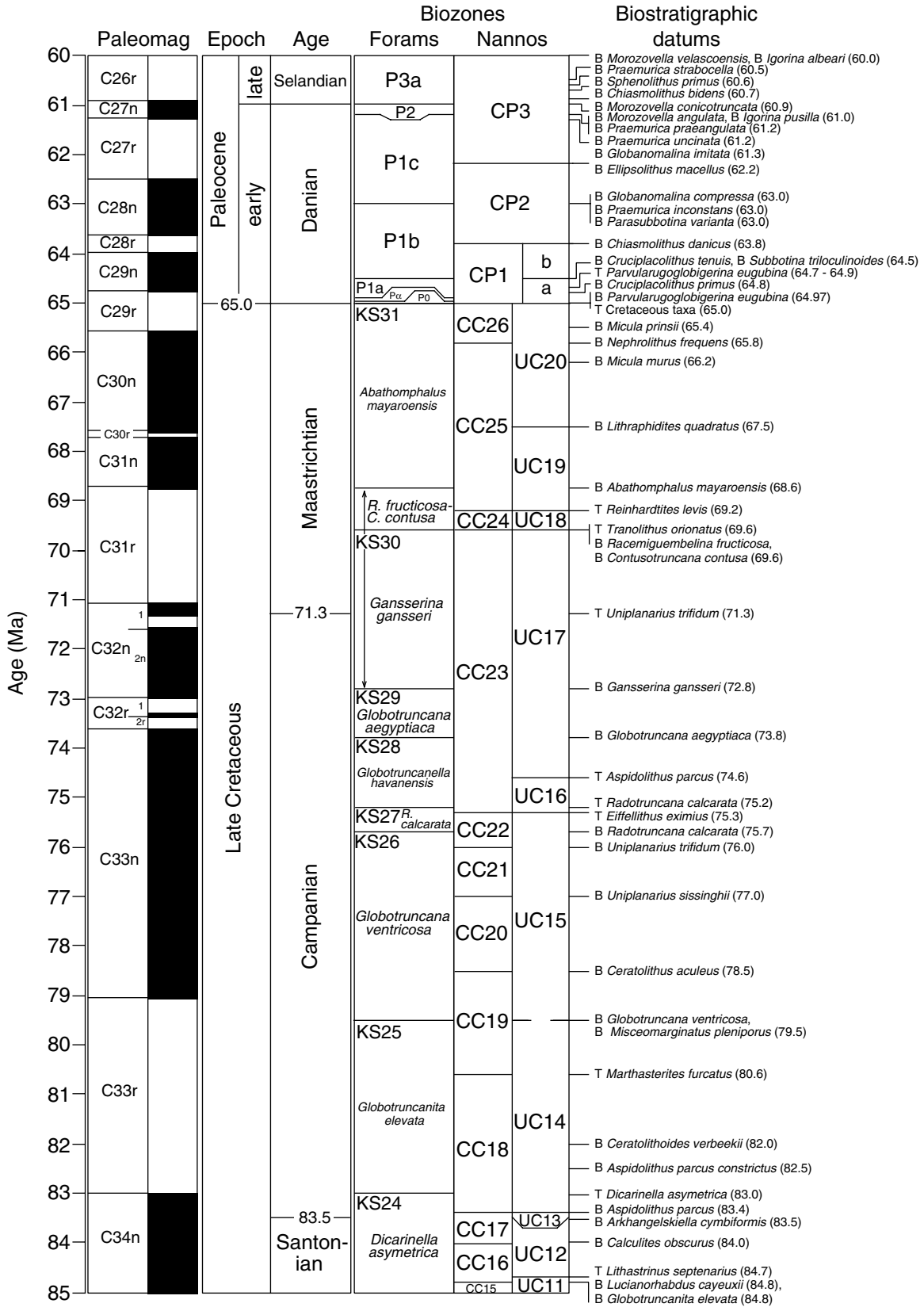

Figure F4 (continued).

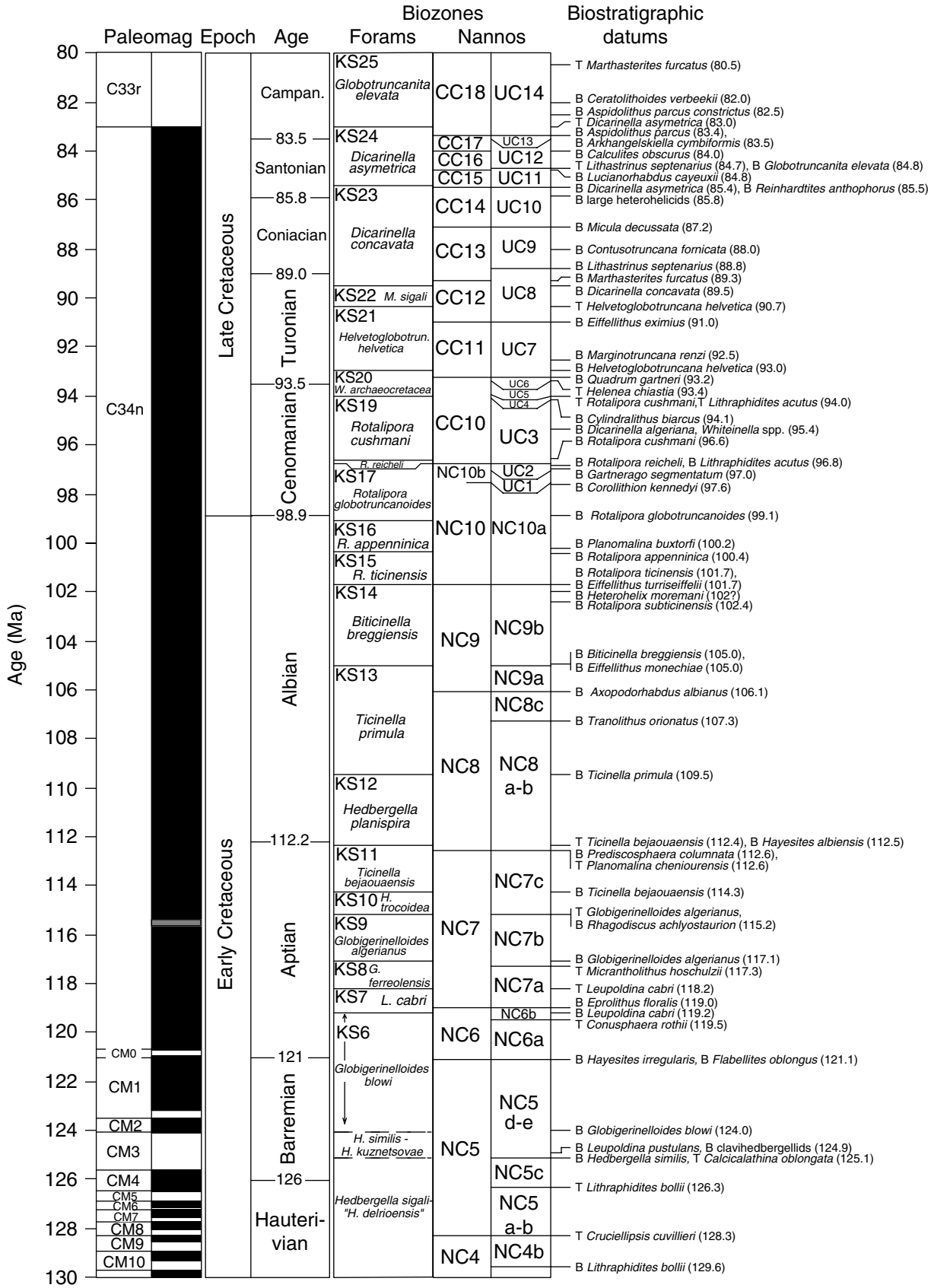

Figure F5. Leg 198 timescale and primary calcareous and siliceous microfossil datums for the Late Jurassic–Early Cretaceous (Gradstein et al., 1995, modified after Channell et al., 1995; and Baumgartner et al., 1995a; Erba et al., 1999; Premoli Silva and Sliter, 1999; A. Bartolini, pers. comm., 2001).

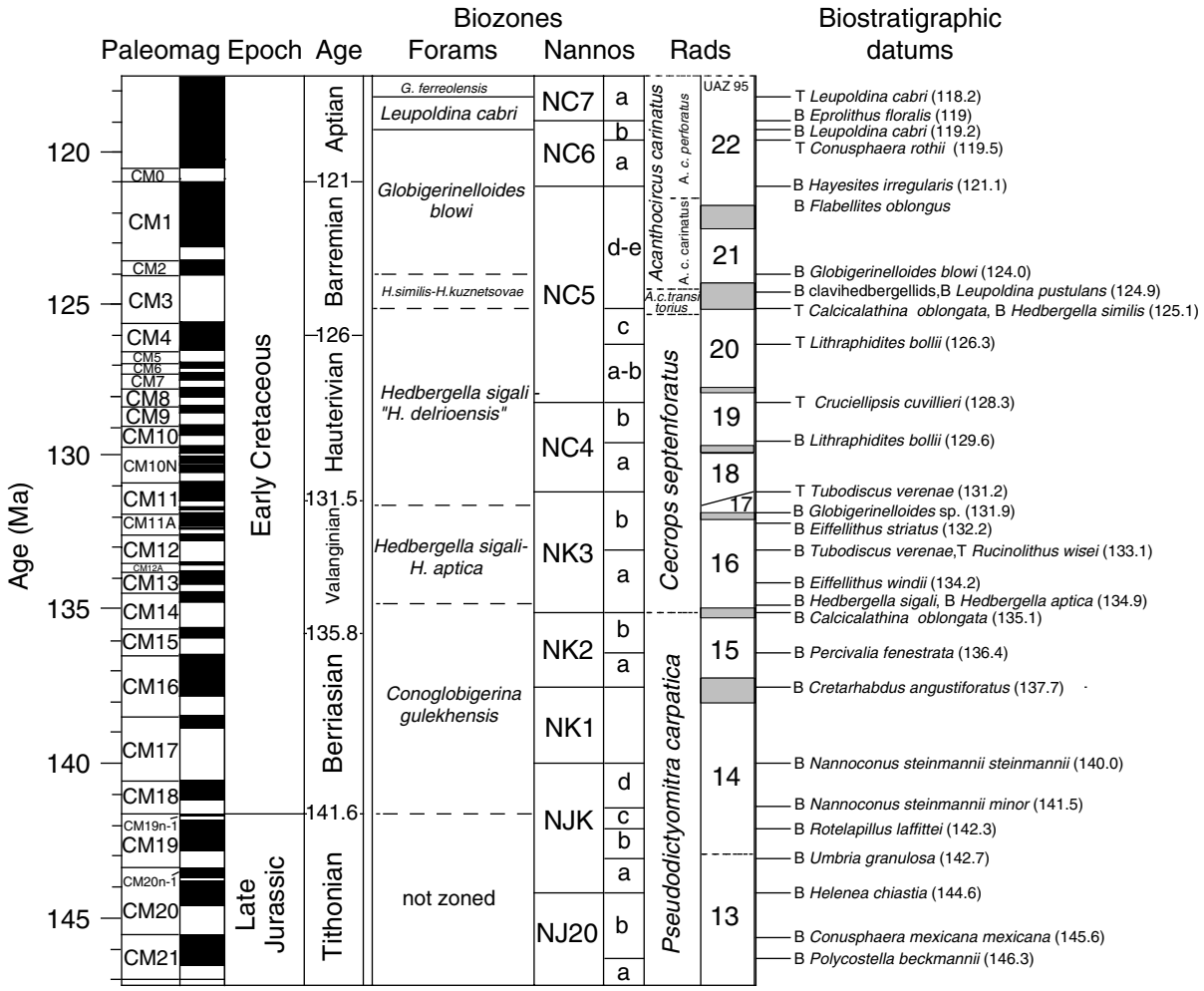

Figure F6. ODP magnetic orientation convention.

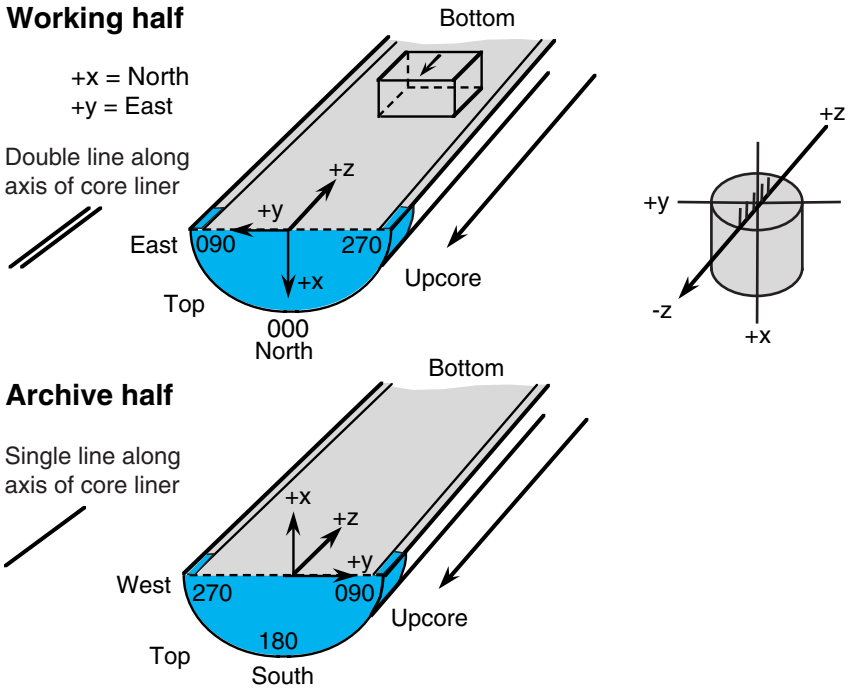

Figure F7. Magnetic susceptibility data. The accurate correction factor for these raw instrument values is 0.68×10^{-5}. **A.** Magnetic susceptibility data from three holes at Site 1211 are shown on the mbsf depth scale. **B.** The same records are shown after depth scale adjustment so that correlative features are aligned. **C.** Resulting spliced record.

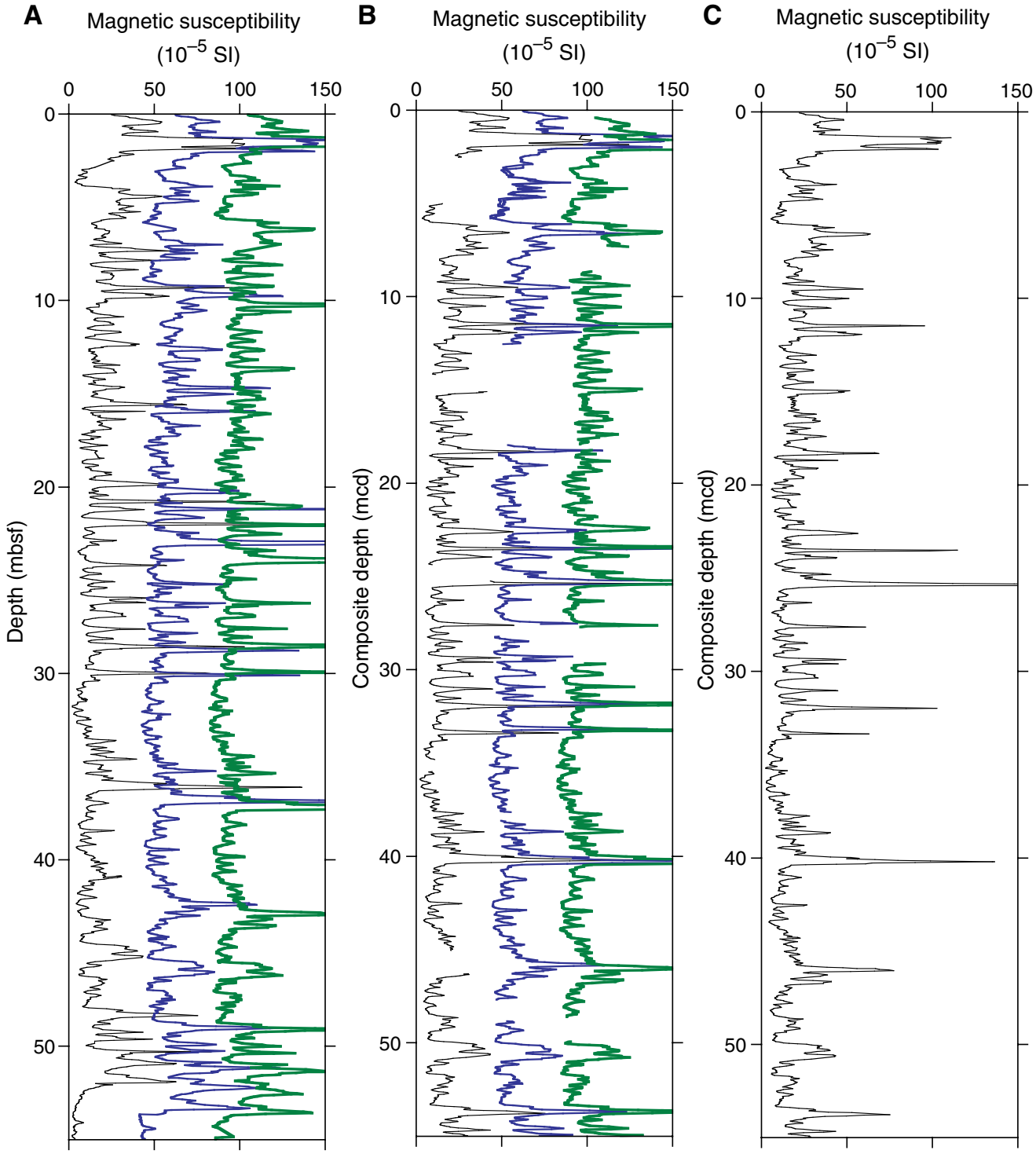

Figure F8. Schematic illustration of the configurations of tool strings run during Leg 198 (see Table T8, p. 63, for explanations of the acronyms).

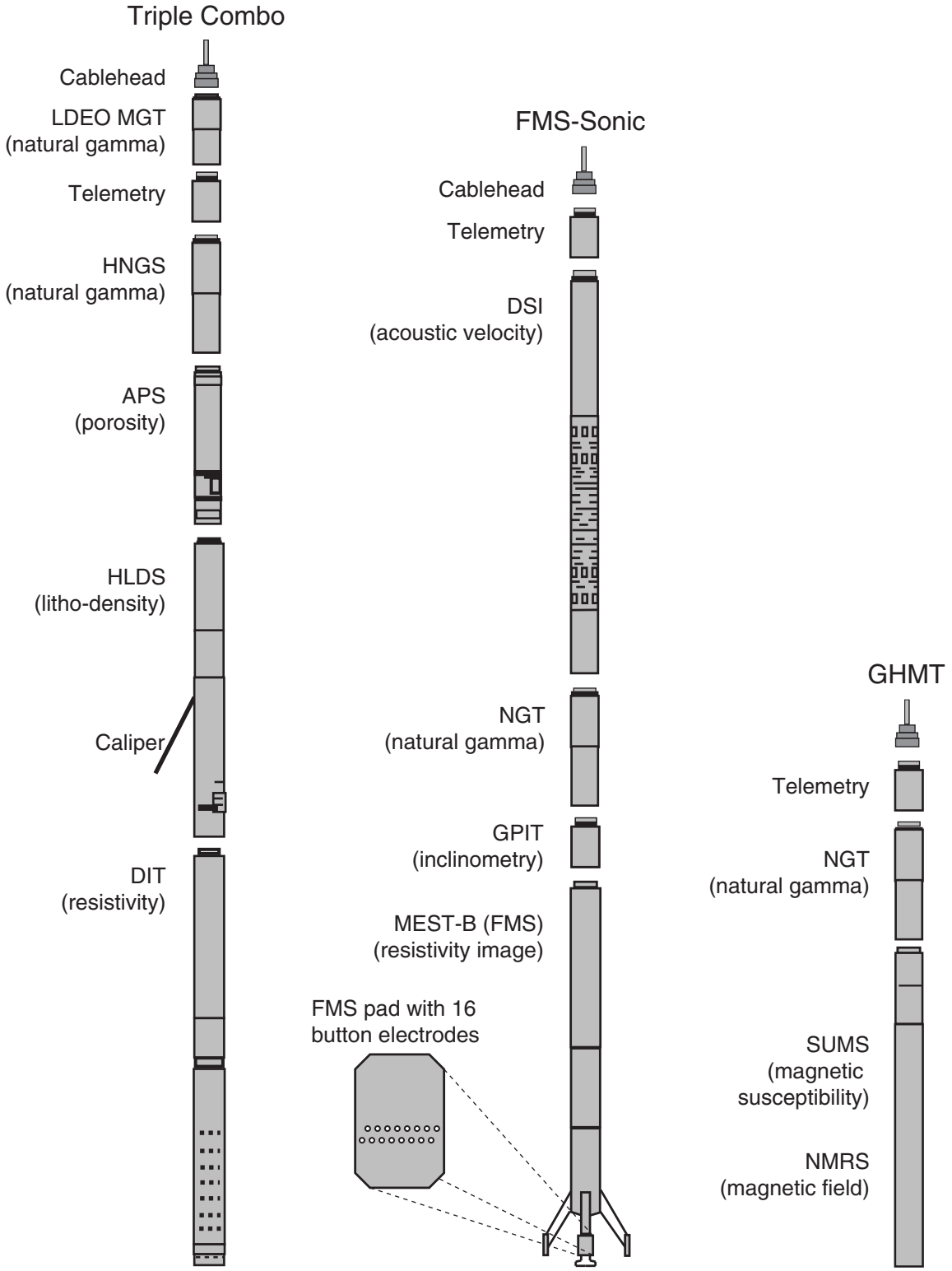

Table T1. Cenozoic calcareous nannofossil datums. (See table notes. Continued on next page.)

Species event	Zone/Subzone (base)	Age (Ma)	Reference
FO *Emiliania huxleyi*	CN15/NN21	**0.26**	1
LO *Pseudoemiliania lacunosa*	CN14b/NN20	**0.46**	1
FO *Gephyrocapsa parallela*	CN14a	0.95	2
FO *Gephyrocapsa caribbeanica*	CN13b	1.73	2
LO *Discoaster brouweri*	CN13a/NN19	**1.95**	1
LO *Discoaster pentaradiatus*	CN12d/NN18	**2.52**	3
LO *Discoaster surculus*	CN12c/NN17	**2.63**	3
LO *Discoaster tamalis*	CN12b	**2.78**	3
LO *Reticulofenestra pseudoumbilicus*	CN12a/NN16	**3.82**	3
LO *Amaurolithus primus*	CN11	**4.56**	3
LO *Ceratolithus acutus*		**5.046**	4
FO *Ceratolithus rugosus*	CN10c/NN13	**5.089**	4
LO *Triquetrorhabdulus rugosus*	CN10b	**5.231**	4
LO *Discoaster quinqueramus*	CN10a/NN12	**5.537**	4
LO *Amaurolithus amplificus*	CN9d/NN11d	**5.999**	4
FO *Amaurolithus amplificus*	CN9c/NN11c	**6.84**	4
FO *Amaurolithus primus*	CN9b	**7.392**	4
FO *Discoaster berggrenii*	CN9a/NN11a	**8.281**	4
FO *Discoaster loeblichii* (*D. neoerectus*?)	CN8b	**8.43**	4
LO *Discoaster hamatus*	CN8a/NN10	**9.635**	4
LO *Catinaster calyculus*		**9.641**	4
LO *Catinaster coalitus*		**9.694**	4
FO *Discoaster neohamatus*		**10.45**	4
FO *Discoaster hamatus*	CN7/NN9a	**10.476**	4
FO *Discoaster brouweri*		**10.687**	4
FO *Catinaster calyculus*		**10.705**	4
FO *Catinaster coalitus*	CN6/NN8	**10.794**	4
LO *Coccolithus miopelagicus*		**10.941**	4
LO *Discoaster kugleri*		**11.52**	4
FO *Discoaster kugleri*	CN5b/NN7	**11.831**	4
LO *Cyclicargolithus floridanus*		**13.19**	5
LO *Sphenolithus heteromorphus*	CN5a/NN6	**13.523**	4
LO *Helicosphaera ampliaperta*	CN4/NN5	15.6	1
LO Acme *Discoaster deflandrei*		**16.2**	5
FO *Sphenolithus heteromorphus*	CN3	18.2	1
FO *Sphenolithus belemnos*	CN2/NN3	19.2	1
FO *Discoaster druggii*	CN1c/NN2	23.2	1
LO *Sphenolithus capricornutus*		23.7	1
LO *Sphenolithus delphix*		23.8	1
LO *Reticulofenestra bisectus*	CN1a–b	23.9	1
FO *Sphenolithus delphix*		24.3	1
LO *Zygrhablithus bijugatus*		24.5	1
LO *Sphenolithus ciperoensis*		25.5	1
LO *Sphenolithus distentus*	CP19b/NP25	27.5	1
FO *Sphenolithus ciperoensis*	CP19a/NP24	29.9	1
FO *Sphenolithus distentus*	CP18	31.5	1
LO *Reticulofenestra umbilicus*	CP17/NP23	32.3	1
LO *Ericsonia formosa*	CP16c/NP22	32.8	1
FO Acme *Ericsonia subdisticha*	CP16b	33.3	1
LO *Discoaster saipanensis*	CP16a/NP21	34.2	1
LO *Discoaster barbadiensis*		34.3	1
FO *Isthmolithus recurvus*	NP19–20	36.0	1
FO *Chiasmolithus oamaruensis*		37.0	1
LO *Chiasmolithus grandis*	CP15/NP18	37.1	1
FO *Reticulofenestra bisectus*		38.0	1
LO *Chiasmolithus solitus*	CP14b/NP17	40.4	1
FO *Cribrocentrum reticulatum*		42.0	1
LO *Nannotetrina fulgens*		43.1	1
FO *Reticulofenestra umbilicus*	CP14a/NP16	43.7	1
LO *Chiasmolithus gigas*	CP13c/NP15c	44.5	1
FO *Chiasmolithus gigas*	CP13b/NP15b	46.1	1
FO *Nannotetrina fulgens*	CP13a/NP15a	47.3	1
FO *Rhabdosphaera inflatus*	CP12b/NP14b	48.5	1
FO *Discoaster sublodoensis*	CP12a/NP14a	49.7	1
LO *Tribrachiatus orthostylus*	CP11/NP13	50.6	1
FO *Toweius crassus*		51.5	1
FO *Discoaster lodoensis*	CP10/NP12	52.85	1
LO *Tribrachiatus contortus*	CP9b/NP11	52.85	1

Table T1 (continued).

Species event	Zone/Subzone (base)	Age (Ma)	Reference
FO *Tribrachiatus orthostylus*		53.6	1
FO *Tribrachiatus contortus*		54.7	1
FO *Discoaster diastypus*	CP9a/NP10	55.0	1
FO *Tribrachiatus bramlettei*	CP9a/NP10	55.0	1
LO *Fasciculithus tympaniformis*		55.3	1
FO *Discoaster multiradiatus*	CP8/NP9	56.2	1
FO *Discoaster okadai*		56.8	1
FO *Discoaster nobilis*	CP7/NP9	56.9	1
FO *Heliolithus riedelii*	NP8	57.3	1
FO *Discoaster mohleri*	CP6/NP7	57.5	1
FO *Sphenolithus anarrhopus*		58.4	1
FO *Heliolithus kleinpellii*	CP5/NP6	58.4	1
FO *Chiasmolithus consuetus*		59.7	1
FO *Fasciculithus tympaniformis*	CP4/NP5	59.7	1
FO *Fasciculithus ulii*		59.9	1
FO *Sphenolithus primus*		60.6	1
FO *Chiasmolithus bidens*		60.7	1
FO *Ellipsolithus macellus*	CP3/NP4	62.2	1
FO *Chiasmolithus danicus*	CP2/NP3	63.8	1
FO *Cruciplacolithus tenuis*	CP1b/NP2	64.5	1
FO *Cruciplacolithus primus*		64.8	1

Notes: FO = first occurrence, LO = last occurrence. Bold = astrochronologically tuned datums. References: 1 = Berggren et al. (1995b), 2 = Kameo and Bralower (2000), 3 = Shackleton et al. (1995), 4 = Backman and Raffi (1997), 5 = Raffi and Flores (1995).

Table T2. Cenozoic planktonic foraminifer datums. (See table notes. Continued on next page.)

Species event	Zone (base)	Age (Ma)	Reference
LO *Truncorotalia tosaensis*	PT1b	**0.65**	1
LO *Globigerinoides fistulosus*	PT1a	**1.88**	3
FO *Truncorotalia truncatulinoides*	N22	**1.92**	3
LO *Globorotalia pseudomiocenica* (Indo-Pacific only)	PL6	**2.3**	2
LO *Globoturborotalia woodi*		**2.33**	3
LO *Dentoglobigerina altispira*	PL5	**3.11**	3
LO *Sphaeroidinellopsis seminulina*	PL4	**3.11**	3
FO *Globigerinelloides fistulosus*		**3.33**	1
FO *Truncorotalia tosaensis*	N21	**3.35**	1
LO *Pulleniatina primalis*		**3.65**	1
LO *Globorotalia margaritae*	PL3	**3.85**	3
FO *Globorotalia crassaformis*		**4.31**	3
LO *Pulleniatina spectabilis*		**4.33**	4
LO *Globoturborotalita nepenthes*	PL2	**4.39**	3
LO *Globorotalia cibaoensis*	PL1b	**4.6**	2
FO *Sphaeroidinella dehiscens* s.l.	N19	**5.20, 5.54**	1, 3
FO *Globorotalia tumida*	N18/PL1a	**5.82**	3
LO *Globorotalia lenguaensis*	M14	6.0	2
FO *Pulleniatina primalis*		6.4	2
FO *Globorotalia conomiozea*		7.12 (6.9)	2
FO *Globigerinoides extremus*		**8.58**	3
FO *Globorotalia plesiotumida*	N17/M13b	**8.58**	3
FO *Neogloboquadrina acostaensis*	N16/M13a	**9.82**	3
LO *Paragloborotalia mayeri*	N15/M12	**10.49**	3
FO *Globoturborotalita nepenthes*	N14/M11	**11.19**	3
LO *Fohsella fohsi* s.l. (incl. *fohsi lobata* and *fohsi robusta*)	N13/M10	**11.68**	3
FO *Globorotalia lenguaensis*		**12.85**	3
FO *Fohsella fohsi robusta*		**13.18**	3
FO *Fohsella fohsi* s.l.	N12/M8	**13.42**	3
FO *Fohsella praefohsi*	N11	14.0	5
FO *Fohsella peripheroacuta*	N10/M7	14.7	5
FO *Orbulina* spp.	N9/M6	15.1	5
FO *Praeorbulina glomerosa*	M5b	16.1	5
FO *Praeorbulina sicana*	N8/M5a	16.4	5
FO *Globorotalia miozea*		16.7	2
LO *Catapsydrax dissimilis*	N7/M4a	17.3	5
FO *Globorotalia praescitula*		18.5	2
FO *Globigerinatella insueta*	N6/M3	18.8	2
LO *Globoquadrina binaiensis*		19.1	5
FO *Globigerinoides altiaperturus*		20.5	2
LO *Paragloborotalia kugleri*	N5/M2	21.5	2
LO *Globigerina angulisuturalis*		21.6	2
FO *Globoquadrina dehiscens*	M1b	23.2	2
FO *Globigerinoides trilobus* s.l.		23.4	5
FO *Paragloborotalia kugleri*	N4/M1a	23.8	2
FO *Globigerinoides primordius* (common)		24.3	2
FO *Paragloborotalia pseudokugleri*		25.9	2
FO *Globigerinoides primordius*		26.7	2
LO *Paragloborotalia opima*	P22	27.1	2
LO *Chiloguembelina cubensis* (common)	P21b	28.5	2
FO *Globigerina angulisuturalis*	P21a	29.4	2
LO *Subbotina angiporoides*		30.0	2
LO *Globigerina ampliapertura*	P20	30.3	2
FO *Paragloborotalia opima*		30.6	2
LO *Pseudohastigerina* spp.	P19	32.0	2
LO *Hantkenina* spp.		33.7	2
LO *Turborotalia cerroazulensis*	P18	33.8	2
LO *Cribrohantkenina inflata*	P17	35.5	2
LO *Globigerinatheka index*		34.3	2
FO *Turborotalia cunialensis*	P16	35.2	2
LO *Turborotalia pomeroli*		35.3	2
LO *Globigerinatheka semiinvoluta*		35.3	2
FO *Cribrohantkenina inflata*		35.5	2
LO *Acarinina collactea*		37.7	2
LO *Subbotina linaperta*		37.7	2
LO *Morozovella spinulosa*		38.1	2
FO *Globigerinatheka semiinvoluta*	P15	38.4	2
LO *Planorotalites* sp.		38.5	2

Table T2 (continued).

Species event	Zone (base)	Age (Ma)	Reference
LO *Acarinina primitiva*		39.0	2
LO *Subbotina frontosa*		39.3	2
LO *"Orbulinoides" beckmanni*	P14	40.1	2
FO *"Orbulinoides" beckmanni*	P13	40.5	2
LO *Acarinina bullbrooki*		40.5	2
FO *Turborotalia pomeroli*		42.4	2
FO *Globigerinatheka index*		42.9	2
FO *Morozovella lehneri*		43.5	2
LO *Morozovella aragonensis*	P12	43.6	2
FO *Globigerinatheka kugleri*	P11	45.8	2
FO *Turborotalia possagnoensis*		46.0	2
FO *Hantkenina nuttalli*	P10	49.0	2
FO *Planorotalites palmerae*	P9	50.4	2
LO *Morozovella formosa*	P8	50.8	2
FO *Acarinina pentacamerata*		50.8	2
FO *Morozovella aragonensis*	P7	52.3	2
LO *Morozovella marginodentata*		52.5	2
LO *Morozovella lensiformis*		52.7	2
LO *Subbotina velascoensis*		53.5	2
LO *Morozovella aequa*		53.6	2
FO *Morozovella formosa*	P6b	54.0	2
FO *Morozovella lensiformis*		54.0	2
LO *Morozovella velascoensis*	P6a	54.7	2
LO *Morozovella acuta*		54.7	2
FO *Morozovella gracilis*		54.7	2
FO *Igorina broedermanni*		54.7	2
FO *Morozovella marginodentata*		54.8	2
FO *Globanomalina australiformis*		55.5	2
FO *Morozovella subbotinae*		55.9	2
LO *Globanomalina pseudomenardii*	P5	55.9	2
LO *Acarinina nitida* (= *A. acarinata*)		56.3	2
LO *Acarinina mckannai*		56.3	2
FO *Acarinina soldadoensis*	P4c	56.5	2
FO *Acarinina coalingensis* (= *triplex*)		56.5	2
FO *Morozovella aequa*		56.5	2
LO *Acarinina subsphaerica*	P4b	57.1	2
FO *Acarinina mckannai*		59.1	2
FO *Acarinina subsphaerica*		59.2	2
FO *Acarinina nitida*		59.2	2
FO *Globanomalina pseudomenardii*	P4a	59.2	2
LO *Parasubbotina variospira* (= *varianta*?)		59.2	2
FO *Morozovella velascoensis*		60.0	2
FO *Igorina albeari*	P3b	60.0	2
FO *Morozovella conicotruncata*		60.9	2
FO *Morozovella angulata*	P3a	61.0	2
FO *Igorina pusilla*		61.0	2
FO *Praemurica praeangulata*		61.2	2
FO *Praemurica uncinata*	P2	61.2	2
FO *Globoanomalina imitata*		61.3	2
FO *Globanomalina compressa*	P1c	63.0	2
FO *Praemurica inconstans*		63.0	2
FO *Parasubbotina varianta*		63.0	2
FO *Subbotina triloculinoides*	P1b	64.5	2
LO *Parvularugoglobigerina eugubina*	P1a	64.9	2
FO *Parvularugoglobigerina eugubina*	Pa	64.97	2

Notes: FO = first occurrence, LO = last occurrence. Bold = astrochronologically tuned datums. References: 1 = Berggren et al. (1995a), 2 = Berggren et al. (1995b), 3 = Chaisson and Pearson (1997), 4 = Shackleton et al. (1995), 5 = Pearson and Chaisson (1997).

Table T3. Cretaceous calcareous nannofossil datums.

Species event	Zone/Subzone (base)	Age (Ma)	References
LO Cretaceous taxa *(Micula prinsii)*		65.0	1
FO *Micula prinsii*		65.4	2
FO *Nephrolithus frequens*	CC26	65.8	2, 3
FO *Micula murus*		66.2	2
FO *Lithraphidites quadratus*	UC20	67.5	2, 4
LO *Reinhardtites levis*	CC25/UC19	69.2	2, 3, 4
LO *Tranolithus orionatus*	CC24/UC18	69.6	2, 3, 4
LO *Uniplanarius trifidum*		71.3	2
LO *Aspidolithus parcus*	UC17	74.6	2, 4
LO *Eiffellithus eximius*	CC23/UC16	75.3	2, 3, 4
FO *Uniplanarius trifidum*	CC22	76.0	2, 3
FO *Uniplanarius sissinghii*	CC21	77.0	2, 3
FO *Ceratolithoides aculeus*	CC20	78.5	2, 3
FO *Misceomarginatus pleniporus*	UC15	79.5	2, 4
LO *Marthasterites furcatus*	CC19	80.6	2, 3
FO *Ceratolithoides verbeekii*		82.0	2
FO *Aspidolithus parcus constrictus*		82.5	2
FO *Aspidolithus parcus*	CC18/UC14	83.4	2, 3, 4
FO *Arkhangelskiella cymbiformis*	UC13	83.5	2, 4
FO *Calculites obscurus*	CC17	84.0	2, 3
LO *Lithastrinus septenarius*	UC12	84.7	2, 4
FO *Lucianorhabdus cayeuxii*	CC16	84.8	2, 3
FO *Reinhardtites anthophorus*	CC15/UC11	85.5	2, 3, 4
FO *Micula decussata*	CC14/UC10	87.2	2, 3, 4
FO *Lithastrinus septenarius*	UC9	88.8	2, 4
FO *Marthasterites furcatus*	CC13	89.3	2, 3
FO *Eiffellithus eximius*	CC12/UC8	91.0	2, 3, 4
FO *Quadrum gartneri*	CC11/UC7	93.2	2, 3, 4
LO *Helenea chiastia*	UC6	93.4	2, 4
LO *Lithraphidites acutus*	UC5	94.0	2, 4
FO *Cylindralithus biarcus*	UC4	94.1	2, 4
FO *Lithraphidites acutus*	CC10/UC3	96.8	2, 3, 4
FO *Gartnerago segmentatum*	UC2	97.0	2, 3, 4
FO *Corollithion kennedyi*	NC10b/UC1	97.6	4, 5, 6
FO *Eiffellithus turriseiffelii*	NC10a	101.7	5, 6
FO *Eiffellithus monechiae*	NC9b	105.0	5, 6
FO *Axopodorhabus albianus*	NC9a	106.1	5, 6
FO *Tranolithus orionatus*	NC8c	107.3	5, 6
FO *Hayesites albiensis*	NC8b	112.5	5, 6
FO *Prediscosphaera columnata*	NC8a	112.6	5, 6
FO *Rhagodiscus achlyostaurion*	NC7c	115.2	5, 6
LO *Micrantholithus hoschulzii*	NC7b	117.3	5, 6
FO *Eprolithus floralis*	NC7a	119.0	5, 6
LO *Conusphaera rothii*	NC6b	119.5	5, 6
FO *Hayesites irregularis*	NC6a	121.1	5, 6
FO *Flabellites oblongus*		121.1	2, 5
LO *Calcicalathina oblongata*	NC5d–e	125.1	2, 5
LO *Lithraphidites bollii*	NC5c	126.3	2, 5
FO *Cruciellipsis cuvillieri*	NC5a–b	128.3	2, 5
FO *Lithraphidites bollii*	NC4b	129.6	2, 5
LO *Tubodiscus verenae*	NC4a	131.2	2, 5
FO *Eiffellithus striatus*		132.2	2, 7
FO *Tubodiscus verenae*	NK3b	133.1	2, 7
LO *Rucinolithus wisei*		133.1	2, 7
FO *Eiffellithus windii*		134.2	2, 7
FO *Calcicalathina oblongata*	NK3a	135.1	2, 7
FO *Percivalia fenestrata*	NK2b	136.4	2, 7
FO *Cretarhabdus angustiforatus*	NK2a	137.7	2, 7
FO *Nannoconus steinmannii steinmannii*	NK1	140.0	2, 7
FO *Nannoconus steinmannii minor*	NJKd	141.5	2, 7
FO *Rotelapillus laffittei*	NJKc	142.3	2, 7
FO *Umbria granulosa*	NJKb	142.7	2, 7
FO *Helenea chiastia*	NJKa	144.6	2, 7
FO *Conusphaera mexicana mexicana*		145.6	2, 7
FO *Polycostella beckmannii*	NJ20b	146.3	2, 7

Notes: FO = first occurrence, LO = last occurrence. References: 1 = Berggren et al. (1995b), 2 = Erba et al. (1995), 3 = Sissingh (1977), 4 = Burnett (1999), 5 = Roth (1973), 6 = Bralower et al. (1997), 7 = Bralower et al. (1989).

Table T4. Cretaceous planktonic foraminifer datums.

Species event	Zone (base)	Age (Ma)	References
LO *Abathomphalus mayaroensis*		65.0	1
FO *Abathomphalus mayaroensis*	*A. mayaroenesis* (KS31)	68.6	2, 3
FO *Racemiguembelina fructicosa*	*R. fructicosa–C. contusa*	69.6	3
FO *Contusotruncana contusa*	*R. fructicosa–C. contusa*	69.6	3
FO *Gansserina gansseri*	*G. gansseri* (KS30)	72.8	2, 4, 5
FO *Globotruncana aegyptiaca*	*G. aegyptiaca* (KS29)	73.8	2, 4, 5
LO *Radotruncana calcarata*	*G. havanensis* (KS28)	75.2	2, 4, 5
FO *Radotruncana calcarata*	*R. calcarata* (KS27)	75.7	2, 4, 5
FO *Globotruncana ventricosa*	*G. ventricosa* (KS26)	79.5	2, 4, 5
LO *Dicarinella asymetrica*	*G. elevata* (KS25)	83.0	2, 4, 5
FO *Globotruncana elevata*		84.8	5
FO *Dicarinella asymetrica*	*D. asymetrica* (KS24)	85.4	2, 4, 5
FO Large heterohelicids		85.8	3
FO *Contusotruncana fornicata*		88.0	3
FO *Dicarinella concavata*	*D. concavata* (KS23)	89.5	2, 4, 5
LO *Helvetoglobotruncana helvetica*	*M. sigali* (KS22)	90.7	2, 4, 6
FO *Marginotruncana* spp. *(M. renzi)*		92.5	3
FO *Helvetoglobotruncana helvetica*	*H. helvetica* (KS21)	93.0	2, 4, 6
LO *Rotalipora cushmani*	*W. archaeocretacea* (KS20)	94.0	2, 4, 6
FO *Dicarinella algeriana*		95.4	3
FO *Whiteinella* spp. *(W. baltica)*		95.4	3
FO *Rotalipora cushmani*	*R. cushmani* (KS19)	96.6	2, 4, 6
FO *Rotalipora reicheli*	*R. reicheli* (KS18)	96.8	2, 4, 6
FO *Rotalipora globotruncanoides*	*R. globotruncanoides* (KS17)	99.1	2, 4, 6
FO *Planomalina buxtorfi*		100.2	7
FO *Rotalipora appenninica*	*R. appenninica* (KS16)	100.4	2, 4, 6
FO *Rotalipora ticinensis*	*R. ticinensis* (KS15)	101.7	2, 4, 6
FO *Heterohelix* spp. *(H. moremani)*		102.0	3, 7
FO *Rotalipora subticinensis*		102.4	2, 4, 6
FO *Biticinella breggiensis*	*B. breggiensis* (KS14)	105.0	2. 4. 6
FO *Ticinella primula*	*T. primula* (KS13)	109.5	2, 4, 6
LO *Ticinella bejaouaensis*	*H. planispira* (KS12)	112.4	2, 4, 6, 7
LO *Planomalina cheniourensis*		112.6	2, 4, 6, 7
FO *Ticinella bejaouaensis*	*T. bejaouaensis* (KS11)	114.3	2, 4, 6, 7
LO *Globigerinelloides algerianus*	*H. trocoidea* (KS10)	115.2	2, 4, 6
FO *Globigerinelloides algerianus*	*G. algerianus* (KS9)	117.1	2, 4, 6
LO *Leupoldina cabri*	*G. ferreolensis* (KS8)	118.2	2, 4, 6
FO *Leupoldina cabri*	*L. cabri* (KS7)	119.2	2, 4, 6
FO *Globigerinelloides blowi*	*G. blowi* (KS6)	124.0	3
FO *Leupoldina pustulans*		124.9	3
FO Clavihedbergellids		124.9	3
FO *Hedbergella similis*	*H. similis–H. kuznetsovae*	125.1	3
FO *Globigerinelloides* spp.	*H. sigali–"H. delrioensis"*	131.9	3
FO *Hedbergella sigali*	*H. sigali–H. aptica*	134.9	3
FO *Hedbergella aptica*		134.9	3

Notes: FO = first occurrence, LO = last occurrence. References: 1 = Berggren et al. (1995b), 2 = Sliter (1989), 3 = Premoli Silva and Sliter (1999), 4 = Caron (1985), 5 = Erba et al. (1995), 6 = Bralower et al. (1997), 7 = Leckie (1984).

Table T5. Example from Site 1209 of a composite depth table.

Core	Depth (mbsf)	Offset (m)	Depth (mcd)
198-1209A-			
1H	0.0	0.00	0.00
2H	8.2	0.08	8.28
3H	17.7	3.06	20.76
4H	27.2	3.67	30.87
5H	36.7	3.86	40.56
6H	46.2	4.71	50.91
7H	55.7	6.01	61.71
8H	65.2	6.59	71.79
9H	74.7	7.62	82.32
10H	84.2	8.29	92.49
11H	93.7	10.18	103.88
12H	103.2	9.36	112.55
13H	112.7	10.42	123.11
14H	122.2	10.19	132.38
15H	131.7	8.31	140.01
16H	141.2	9.57	150.77
17H	150.7	11.24	161.94
18H	160.2	10.98	171.18
19H	169.7	12.53	182.23
20H	179.2	12.15	191.35
21H	188.7	13.21	201.90
22H	198.2	14.20	212.40
23H	207.7	15.65	223.35
24H	217.2	15.03	232.23
25H	226.7	16.28	242.97
26H	236.2	16.45	252.65
27X	245.7	16.45	262.15
28X	250.9	16.45	267.35
198-1209B-			
1H	0.0	0.12	0.12
2H	5.1	–0.06	5.04
3H	14.6	0.61	15.21
4H	24.1	1.49	25.59
5H	33.6	3.72	37.32
6H	43.1	5.92	49.02
7H	52.6	6.11	58.71
8H	62.1	6.57	68.67
9H	71.6	7.63	79.23
10H	81.1	7.73	88.83
11H	90.6	10.13	100.73
12H	100.1	10.86	110.96
13H	109.6	9.86	119.46
14H	119.1	10.26	129.36
15H	128.6	10.96	139.56
16H	138.1	9.39	147.49
17H	147.6	10.83	158.43
18H	157.1	11.62	168.72
19H	166.6	12.06	178.66
20H	176.1	11.95	188.05
21H	185.6	13.52	199.12
22H	195.1	14.81	209.91
23H	204.6	15.66	220.26
24H	214.1	14.89	228.99
25H	223.6	16.47	240.07
26H	233.1	18.74	251.84
27H	242.6	18.74	261.34
28H	252.1	18.74	270.84
29H	261.6	18.74	280.34
30H	271.1	18.74	289.84
31H	280.6	18.74	299.34
32H	290.1	18.74	308.84
33H	297.6	18.74	316.34
198-1209C-			
1H	98.0	9.66	107.66
2H	107.5	9.81	117.31
3H	117.0	11.34	128.34
4H	126.5	10.45	136.95
5H	136.0	8.76	144.76
6H	145.5	9.73	155.23
7H	155.0	11.62	166.62
8H	164.5	12.12	176.62
9H	174.0	13.06	187.06
10H	183.5	15.29	198.79
11H	193.0	13.91	206.91
12H	202.5	15.57	218.07
13H	212.0	16.84	228.84
14H	221.5	16.16	267.66
15H	231.0	16.63	214.37
16H	240.5	16.63	257.13
17H	250.0	16.63	266.63
18H	252.5	16.63	269.13
19H	262.0	16.63	278.63
20H	268.4	16.63	285.03
21H	277.9	16.63	294.53
22H	287.4	16.63	287.40
23X	299.7	16.63	316.33

Table T6. Measured parameters, analytical methods, and reproducibility of results for Leg 198 interstitial water geochemistry.

Parameter	Method	Reproducibility
Alkalinity	Gran titration	±1.5%
Cl^-	Titration with AgCl	±0.1%
K^+	Ion chromatography	±0.02%
Mg^{2+}	Ion chromatography	±0.1%
Ca^{2+}	Ion chromatography	±0.2%
SO_4^{2-}	Ion chromatography	±0.1%
$Si(OH)_4$	Spectrophotometry	±2 µm
NH_4^+	Spectrophotometry	±4 µm
HPO_4^{2-}	Spectrophotometry	±0.2 µm
Fe^{2+}	ICP-AES	±2.3%
Mn^{2+}	ICP-AES	±2.3%
H_3BO_3	ICP-AES	±2.4%
Li^+	ICP-AES	±4.4%
Sr^{2+}	ICP-AES	±1.0%
Ba^{2+}	ICP-AES	±1.1%

Note: ICP-AES = inductively coupled plasma–atomic emission spectroscopy.

Table T7. Measurements made by wireline tool strings.

Tool string*	Tool†	Measurement	Sampling interval (cm)	Approximate vertical resolution (cm)
Triple combination	HNGS‡	Spectral gamma ray	15	51
	APS	Porosity	5 and 15	43
	HLDS	Bulk density	2.5 and 15	38/46
	DIT	Resistivity	15	200/150/76
	MGT**	Gamma ray	15	15
Formation MicroScanner (FMS)-sonic combination	NGT	Spectral gamma ray	15	46
	GPIT	Tool orientation	0.25 and 15	NA
	FMS	Microresistivity	0.25	0.5
	DSI	Acoustic velocity	15	107
GHMT	NGT	Spectral gamma ray	15	46
	SUMS	Susceptibility	5 and 15	35
	NMRS	Total field	5 and 15	45

Notes: * = all tool and tool string names (except the TAP and MGT tools) are trademarks of Schlumberger. † = for additional information about tool physics and use consult ODP Logging Services at **http://www.ldeo.columbia.edu/BRG/ODP.** ‡ = see Table **T8,** p. 63, for explanations of acronyms used to describe tool strings and tools. ** = not included in each logging run. NA = not applicable.

Table T8. Acronyms and units used for wireline tools.

Tool	Output	Explanation	Unit
APS		Accelerator porosity sonde	
	APLC	Near array porosity (limestone calibrated)	%
	SIGF	Formation capture cross section (Σ_f)	Capture units
	STOF	Tool standoff (computed distance from borehole wall)	in
DIT		Dual induction tool	
	IDPH	Deep induction resistivity	Ωm
	IMPH	Medium induction resistivity	Ωm
	SFLU	Spherically focused resistivity	Ωm
DSI		Dipole sonic imager	
	DTCO	Compressional wave delay time (Δt)	ms/ft
	DTSM	Shear wave delay time (Δt)	ms/ft
	DTST	Stoneley wave delay time (Δt)	ms/ft
FMS		Formation MicroScanner	
	C1, C2	Orthogonal hole diameters	in
	P1AZ	Pad 1 azimuth	Degrees
		Spatially oriented resistivity images of borehole wall	
GHMT		Geologic high-resolution magnetic tool	
	MAGS	Magnetic susceptibility (limited range)	ppm
	RMGS	Low-resolution magnetic susceptibility (wider range)	ppm
	MAGC	Earth's conductivity	ppm
	MAGB	Earth's total magnetic field	nT
GPIT		General purpose inclinometer tool	
	DEVI	Hole deviation	Degrees
	HAZI	Hole azimuth	Degrees
	Fx, Fy, Fz	Earth's magnetic field (three orthogonal components)	Degrees
	Ax, Ay, Az	Acceleration (three orthogonal components)	m/s^2
HLDS		Hostile environment lithodensity sonde	
	RHOM	Bulk density	g/cm^3
	PEFL	Photoelectric effect	b/e^-
	LCAL	Caliper (measure of borehole diameter)	in
	DRH	Bulk density correction	g/cm^3
HNGS		Hostile environment gamma ray sonde	
	HSGR	Standard (total) gamma ray	gAPI
	HCGR	Computed gamma ray (HSGR minus uranium contribution)	gAPI
	HFK	Potassium	wt%
	HTHO	Thorium	ppm
	HURA	Uranium	ppm
MGT		Multisensor gamma tool	
	GR	Gamma ray	gAPI
NGT		Natural gamma ray spectrometry tool	
	SGR	Standard total gamma ray	gAPI
	CGR	Computed gamma ray (SGR minus uranium contribution)	gAPI
	POTA	Potassium	wt%
	THOR	Thorium	ppm
	URAN	Uranium	ppm